

<https://doi.org/10.1038/s44303-024-00052-0>

High speed innovations in photoacoustic microscopy

**Xiaoyi Zhu, Luca Menozzi, Soon-Woo Cho & Junjie Yao**

Photoacoustic microscopy (PAM) is a key implementation of photoacoustic imaging (PAI). PAM merges rich optical contrast with deep acoustic detection, allowing for broad biomedical research and diverse clinical applications. Recent advancements in PAM technology have dramatically improved its imaging speed, enabling real-time observation of dynamic biological processes *in vivo* and motion-sensitive targets *in situ*, such as brain activities and placental development. This review introduces the engineering principles of high-speed PAM, focusing on various excitation and detection methods, each presenting unique benefits and challenges. Driven by these technological innovations, high-speed PAM has expanded its applications across fundamental, preclinical, and clinical fields. We highlight these notable applications, discuss ongoing technical challenges, and outline future directions for the development of high-speed PAM.

Photoacoustic imaging (PAI) is increasingly used in biomedical research and clinical diagnostics. PAI stands out by merging the rich contrast of optical imaging with the deep penetration of ultrasound imaging. This synergy complements conventional imaging technologies, providing a powerful tool for improved diagnostic precision and treatment guidance. PAI stems from the photoacoustic effect¹, where absorbed photon energy is partially converted into acoustic waves. In PAI, short laser pulses irradiate the biological tissues, and the absorbed photon energy induces a transient thermoelastic expansion, generating ultrasonic waves. These ultrasonic waves, known as photoacoustic waves, propagate through the tissue and are subsequently detected by ultrasonic transducers. The data collected from these waves are used to reconstruct the distribution of optical absorption contrast within the tissue. Due to its inherent optical contrast, PAI can provide detailed anatomical, functional, and molecular information. Meanwhile, the technique benefits significantly from the minimal scattering of ultrasound waves within biological tissues, enabling PAI to produce high-resolution images with deeper penetration than traditional optical imaging modalities.

PAI has developed into a large family of imaging techniques over the past two decades, finding both preclinical and clinical applications. However, much of the history of photoacoustic technologies was in applications unrelated to imaging². The photoacoustic effect was first discovered by Alexander Graham Bell in the late 19th century, and early efforts were made in using it for wireless communication purposes³. The first half of the 20th century saw applications in photoacoustic gas spectroscopy⁴, which, however, was superseded by gas chromatography developed in the 1950s. The development of laser technology in 1960 led to another advance in photoacoustic research, as lasers were more powerful and stable as a light source. The following decades saw the development of photoacoustic spectroscopy

for biological materials⁵ and imaging of inorganic materials⁶. The first laser-induced photoacoustic images were produced in the 1990s⁷, which set the stage for an explosion of development and applications of photoacoustics to biological imaging in the early 2000s.

PAI is typically grouped into two principal forms: photoacoustic computed tomography (PACT) and photoacoustic microscopy (PAM)⁸. PACT typically uses diffuse optical illumination coupled with parallel detection of acoustic waves by a multi-element transducer array⁹. An inverse reconstruction algorithm is then used to reconstruct the tomographic optical absorption image. It is particularly effective for imaging deep tissues in real-time, making it a valuable tool in a wide range of preclinical applications¹⁰, such as imaging the breast cancer¹¹, prostate cancer¹², or melanomas¹³. While PACT is effective at imaging deeper tissues, its resolution is relatively poor (generally 200–500 μm). By contrast, PAM is favored for studies that require detailed visualization of tissue morphology and function at the microscopic level¹⁴. In a traditional PAM setup, optical illumination and acoustic detection are confocally aligned and mechanically scanned point-by-point over the target tissue. At each scanning position, the dual optical and acoustic foci jointly provide the lateral resolution while the acoustic time-of-flight offers the depth information. Unlike PACT, which applies a reconstruction algorithm to the acquired data to create an tomographic image, PAM directly forms images from the depth-resolved signals¹⁴, known as A-lines. By acquiring A-lines along one lateral dimension of a target, a 2D image (B-scan) can be generated, and similarly by raster scanning along two lateral dimensions of a target, a three-dimensional volume (C-scan) can be generated. PAM can be further implemented as two distinct types based on the focusing mechanisms: Optical-Resolution PAM (OR-PAM) and Acoustic-Resolution PAM (AR-PAM). OR-PAM achieves higher resolution by employing tightly focused optical beams, typically

Table 1 | Imaging performance of different scanning mechanisms for high-speed PAM

Scanning mechanisms	Scanning speed			Scanning range	Lateral Resolution	Pixel Number	Ref.
	Laser PRF	Bscan	C-scan				
Voice-coil	4 kHz	20 Hz 40 Hz	-	9 mm 1 mm	3.4 μ m	-	19
Galvanometer	50 kHz	250 Hz	0.5 Hz	$4 \times 8 \text{ mm}^2$	6 μ m	200 \times 500	23
	500 kHz	500 Hz	2.5 Hz	2.4 mm	7.5 μ m	500	24
1-axis MEMS	100 kHz	400 Hz	0.8 Hz	$2 \times 5 \text{ mm}^2$	2.4 μ m	-	26
2-axis MEMS	50-kHz	35 Hz	0.05 Hz	$2 \times 2 \text{ mm}^2$	12 μ m	700 \times 700	28
Polygon scanner	600 kHz	900 Hz	1/16 Hz	$12 \times 20 \text{ mm}^2$	8.8 μ m	-	30
	800 kHz	1 kHz	2 Hz	$11 \times 7.5 \text{ mm}^2$	10 μ m	250 \times 250	63

Note: “-” indicates information not available

more than ten times finer than the acoustic focus, making it particularly effective for high-resolution imaging of superficial tissues by using (quasi) ballistic photons (imaging depth: $<1 \text{ mm}$)¹⁵. In contrast, AR-PAM utilizes tighter acoustic focusing with optical focusing, making it advantageous for deeper tissue penetration due to its reliance on diffused photons rather than ballistic photons (imaging depth $>3 \text{ mm}$)¹⁶.

Traditional PAM systems (OR-PAM and AR-PAM) rely on motorized scanning stages for point-by-point raster scanning^{15,17}, and have been limited by their slow imaging speeds. This limitation has restricted their ability to capture rapid biological processes such as changes in blood flow and oxygen saturation. Recent technological breakthroughs have led to the development of high-speed PAM technologies that greatly improve temporal resolution and high-speed imaging capabilities. These innovations enable detailed visualization of biological structures and functions at unprecedented speeds, broadening the potential applications of PAM. This review summarizes these technological advancements and discusses the ongoing and prospective applications of high-speed PAM in both biomedical and preclinical settings.

Advances in high-speed PAM

We classify high-speed PAM into three categories based on the method of excitation and detection: a single excitation laser beam with a single-element ultrasound detector, multiple excitation laser beams with a single-element ultrasound detector, and multiple excitation laser beams with parallel ultrasound detection.

A single excitation laser beam with a single-element ultrasound detector

The traditional PAM system is based on a single laser beam excitation and a single-element ultrasound detector. Maslov et al. developed the first-generation OR-PAM system¹⁵ and Zhang et al.¹⁶ developed the first-generation AR-PAM system. For both systems, the data acquisition involves scanning the focused laser beam and a single-element ultrasound detector to detect the resultant photoacoustic signals point-by-point. The laser's pulse repetition frequency (PRF) determines the time interval between consecutive A-line acquisitions. In the past decade, high-repetition-rate diode-pumped lasers have been successfully implemented to improve the PAM speed^{9,12,18}. Along with these advancements in laser technology, extensive studies on new scanning and detection mechanisms have significantly enhanced the performance of high-speed PAM, which will be discussed in the following sections.

Advances in scanning mechanism

The initial PAM systems mechanically scan either the imaging head or the imaged target, which has low efficiency. To improve the speed, combined optical-acoustic scanning has emerged as a promising alternative. These systems employ fast, synchronized scanning of both the optical and acoustic beams. For example, Wang et al. developed a fast PAM system with a mechanical scanning device that uses a voice-coil translation stage. It has

achieved up to a 40 Hz B-scan rate over a 1 mm scanning range with a lateral resolution of 3.4 μ m. However, this method is limited in further increase in imaging speed due to the limited driving force and the weight of the imaging head¹⁹. Since the mechanical scanning of the entire ultrasound detector and light-guiding elements limit the imaging speed^{19–21}, water-immersible scanning mirrors have become a popular alternative. These mirrors can deflect both the laser beam and acoustic beam, providing a much more effective mechanism for scanning both beams simultaneously, without the need for scanning the bulky optical or acoustic components. So far, there have been three main water-immersible scanning systems explored for high-speed PAM: (1) the galvanometer scanner, (2) the micro-electro-mechanical system (MEMS) scanner, and (3) the polygon-mirror scanner. The performance of different scanning methods for high-speed PAM is summarized in Table 1.

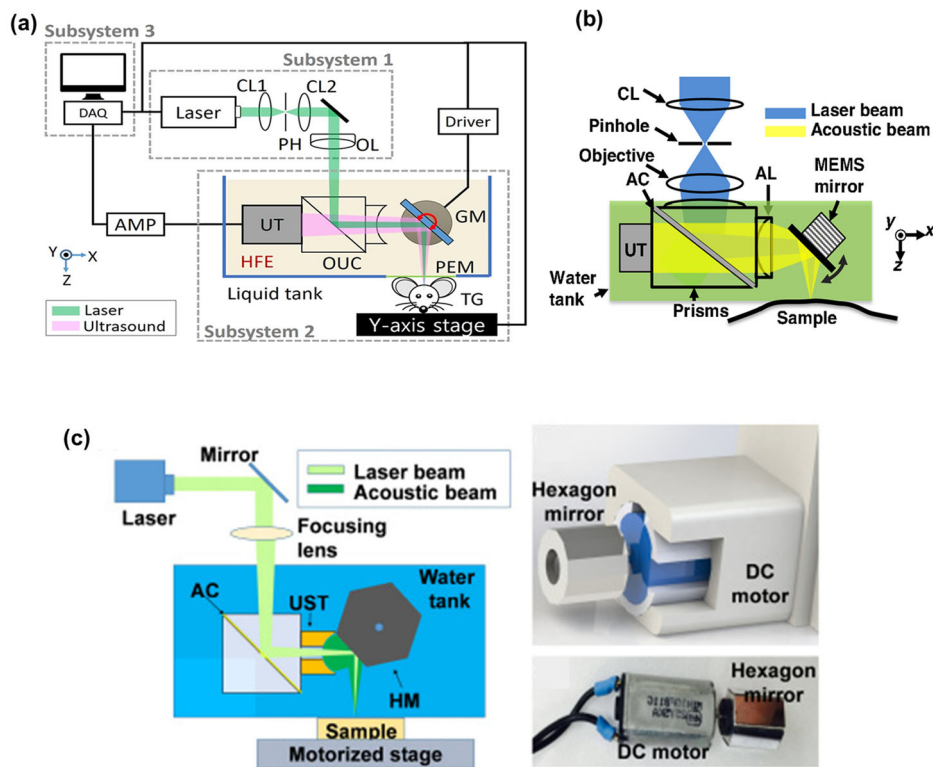
Galvanometer scanner

Galvanometer scanners have been widely used in conventional optical microscopy systems with the advantages of high stability, high precision, and high speed. Because galvanometers generally cannot operate in water, they have typically been used in OR-PAM for optical scanning only in the air^{18,22}, which limits the ability to coaxially scan both the optical and acoustic beams. Without coaxial alignment between light and ultrasound, these OR-PAM systems suffer from low signal-to-noise ratio (SNR) and/or a small field-of-view (FOV). To overcome this challenge, Kim et al.²³ presented a high-speed OR-PAM system based on a galvanometer immersed in non-conducting liquid to enable both acoustic and optical scanning (Fig. 1a). Using an opto-ultrasound beam combiner, this OR-PAM system takes 2 s to acquire volumetric data with a wide FOV of $4 \times 8 \text{ mm}^2$. The measured lateral and axial resolutions were 6.0 and 37.7 μ m, respectively. In a follow-up study²⁴, Kim et al. placed the galvanometer scanner vertically to keep the driving system out of the water while the scanning mirror in the water, achieving a semi-water-immersible galvanometer scanner. This arrangement enables the scanner to steer both the exciting optical beam and emitted acoustic beam simultaneously. With the enhanced galvanometer scanner, the temporal resolution was improved to a B-scan rate of 500 Hz with a lateral resolution of 7.5 μ m, a scanning range of $\sim 2.4 \text{ mm}$, and a laser PRF of 500 kHz. Additionally, Lee et al.²⁵ presented a waterproof galvanometer scanner mounted on a custom-designed water barricading structure, and achieved a $9.0 \times 14.5 \text{ mm}^2$ scanning region, with an A-line rate of 40 kHz, and a lateral resolution of 4.9 μ m. Galvanometer scanners are widely available commercial products and have demonstrated reliable performance compared to MEMS scanners and polygon-mirror scanners (to be discussed below). However, the tradeoff between the speed and FOV remains a limitation for Galvanometer-based high-speed PAM.

Water-immersible MEMS scanner

Water-immersible MEMS scanners have been instrumental in advancing high-speed PAM due to their miniature size, fast response, cost-efficiency, and most importantly, high compatibility with water environment. In 2012,

Fig. 1 | High-speed PAM based on water-immersible scanners. **a** Schematic of the galvanometer-scanner-based OR-PAM with the galvanometer in a non-conducting liquid. GM, galvanometer; OUC, opto-ultrasound combiner; UT, ultrasound transducer; CL, condenser lens; OL, objective lens; PH, pinhole; PEM, polyethylene membrane; TG, target. (adapted with permission from ref. 23). **b** Schematic of a MEMS-scanner-based OR-PAM system. CL, condenser lens; AC, aluminum coating; AL, acoustic lens; UT, ultrasonic transducer (adapted with permission from ref. 26). **c** Schematic of a polygon-scanner based OR-PAM system (left). AC, aluminum coating; HM, hexagon mirror; UST, ultrasonic transducer. The 3D drawing and photograph of the hexagon scanning mirror driven by a high-speed DC-motor are also shown (adapted with permission from ref. 30).



Yao et al.²⁶ were first to develop high-speed OR-PAM based on a water-immersible MEMS scanner (Fig. 1b) that significantly increased the B-scan speed to 400 Hz, although initially limited to single-axis operation which required additional motorized scanning for C-scans. In 2015, this method was advanced by Kim et al.²⁷ by the demonstration of a two-axis MEMS scanner, improving scanning rates to 50 Hz and 30 Hz in the X and Y directions, respectively, which enabled them to monitor the flow of carbon particles at a C-scan rate of 0.25 Hz. Park et al.²⁸ and Chen et al.²⁹ further improved this technology by developing compact handheld probes that integrated two-axis MEMS scanners, capable of supporting higher C-scan rates with a wider FOV. The use of water-immersible MEMS scanners facilitated faster imaging, broadened the FOV, and improved confocal alignment (resulting in higher sensitivity). Despite these advancements, several challenges for MEMS-based PAM systems remain, such as the durability of the mirrors and image distortion due to unstable underwater scanning patterns. Ongoing efforts are focused on refining this technology for long-term use and enhancing image quality. Nevertheless, one common significant drawback of MEMS scanners is the heavy dependence of the scanning range on the resonant scanning frequencies, which limits its flexibility of tuning the scanning range and the imaging speed for different applications.

Polygon-mirror scanner

The polygon-mirror scanner is well-suited for high-speed imaging, without the limitation of MEMS scanners. Lan et al. developed a wide-field OR-PAM system that utilizes a water-immersible polygon-mirror scanner steered by a high-precision DC motor (Fig. 1c)³⁰. This system achieved a B-scan rate of 900 Hz over a 12 mm scanning range while maintaining confocal alignment of the optical and acoustic beams. The volumetric imaging speed over a $1 \times 1 \text{ cm}^2$ region is 3900 times faster than that of the second-generation OR-PAM system¹⁷, 300 times faster than the voice-coil-based OR-PAM¹⁹, and at least 10 times faster than the MEMS-based OR-PAM³¹. For high-speed PAM, a rotating polygon mirror is favored over the vibrational MEMS and Galvanometer scanners for its simplicity and robustness, requiring no oscillating components or complex driving systems. However, when

immersed in water for acoustic coupling, the water-damping force may cause the polygon to wobble. Additionally, size variations in the facets can lead to misaligned scanning trajectories, resulting in distorted B-scans. To address these issues, facet co-registration and upsampling are needed to improve the image quality. Alternatively, the polygon scanner can be operated in the air to steer only the laser beam for high-speed PAM, while the focused ultrasound detection is performed by a cylindrically focused transducer³². Doing so, the polygon scanning speed can be further improved with better scanning stability.

Advances in detection mechanism

In traditional PAM systems, piezoelectric ultrasound transducers are commonly used for signal detection. However, these opaque transducers present several challenges, such as blocking the optical path, being bulky and cumbersome, and complicating the alignment of optical and acoustic beams. These issues can partially limit the imaging speed, FOV, and the SNR. To address these limitations, optically transparent ultrasonic detectors have been developed, allowing excitation light to pass directly through the detectors. In recent years, several types of transparent detectors have been reported for high-speed PAM, including transparent piezoelectric ultrasonic detectors and optical ultrasonic detectors.

Transparent piezoelectric ultrasonic detectors

In traditional PAM systems, piezoelectric-based ultrasound detectors are the most commonly used. These detectors typically consist of an active piezoelectric layer, acoustic matching layers, backing material, an acoustic lens, and electrodes. To develop a transparent sensor, all these components must maintain high transparency across a broad range of optical wavelengths^{33–35}. Currently, widely used transparent piezoelectric ceramic materials include Lithium Niobate (LNO)^{36–40}, Lead Magnesium Niobate-Lead Titanate (PMN-PT)^{41–43}, and Polyvinylidene Difluoride (PVDF)^{44,45}.

LNO is particularly well-suited for high-speed, high-frequency PAM imaging due to its excellent transparency and robust piezoelectric properties. Chen et al.³⁸ demonstrated a high-speed, wide-field OR-PAM system utilizing a cylindrically-focused transparent LNO ultrasound transducer

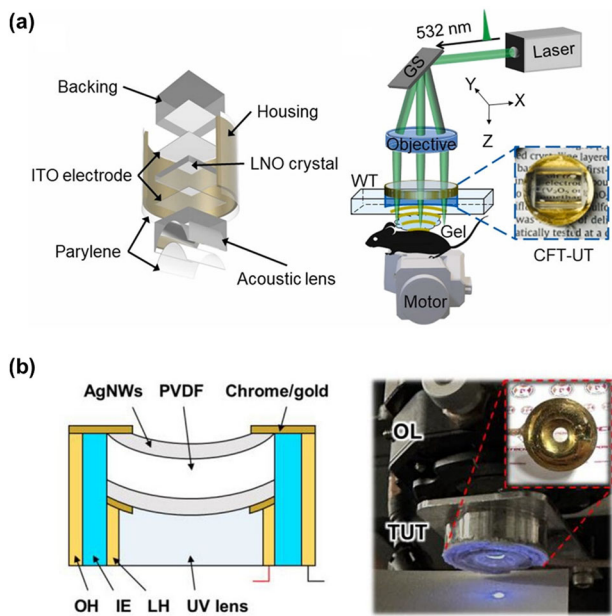


Fig. 2 | Transparent piezoelectric ultrasonic detectors for PAM. **a** Structure of the cylindrically-focused transparent ultrasound transducer (CFT-UT) (shown on the left) and the system schematic of CFT-UT PAM (shown on the right). LNO, lithium niobate; GS, galvo scanner; Gel, ultrasound gel; WT, water tank. The inset photo shows the fabricated CFT-UT (adapted with permission from ref. 38). **b** A cross-sectional structure of the UV-TUT (shown on the left) and photograph of the UV-TUT, demonstrating its UV transparency (shown on the right). Red dashed box outlines a photograph of the UV-TUT. TUT, transparent ultrasound transducer; AgNWs, silver nanowires; LH, lens housing; OH, outer housing; IE, insulating epoxy; and OL, objective lens (adapted with permission from ref. 45).

(Fig. 2a). This transducer features transparent LNO as the active material, coated with indium-tin-oxide electrodes, and is equipped with a transparent cylindrical lens that forms a 9 mm acoustic focal line. The design allows for a reflection-mode imaging setup, where the excitation light passes directly through the transducer. By rapidly scanning the focused excitation light along the acoustic focal line and maintaining confocal alignment between optical excitation and acoustic detection, the system achieves consistent detection sensitivity over the entire scanning range. This system can produce cross-sectional images at a frame rate of 500 Hz.

PVDF, while flexible and suitable for wide-bandwidth applications, is generally limited by its lower piezoelectric efficiency and sensitivity. However, its application in high-resolution imaging is promising. Kim et al.⁴⁵ introduced an ultraviolet-transparent ultrasound transducer designed for high-resolution reflection-mode UV-PAM (Fig. 2b). This transducer utilizes PVDF film as the piezoelectric material, with silver nanowires (AgNWs) serving as transparent electrodes. The design achieves a light transmission efficiency of 61.1% at 266 nm and offers acoustic performance that is four times higher than that of conventional ring-shaped ultrasound transducers. With this transducer, they developed a reflection-mode UV-PAM system capable of achieving a numerical aperture (NA) of 0.38 and delivering a lateral resolution of $0.47 \pm 0.03 \mu\text{m}$. The system was used for photoacoustic histopathology of cancerous tissues.

Optical ultrasonic detectors

Despite ongoing research into transparent piezoelectric ultrasound transducers, some challenges remain, including issues with transparency, sensitivity, and bandwidth. As an alternative, optical-detection-based ultrasound transducers have been applied to high-speed PAM^{46–48}. Fiber-optic ultrasound sensors have become popular in PAI^{46,47}. Instead of scanning both optical beams and acoustic waves, these PAM systems scan the optical beam only and keep the acoustic detection stationary. Zhang et al.^{49,50} developed

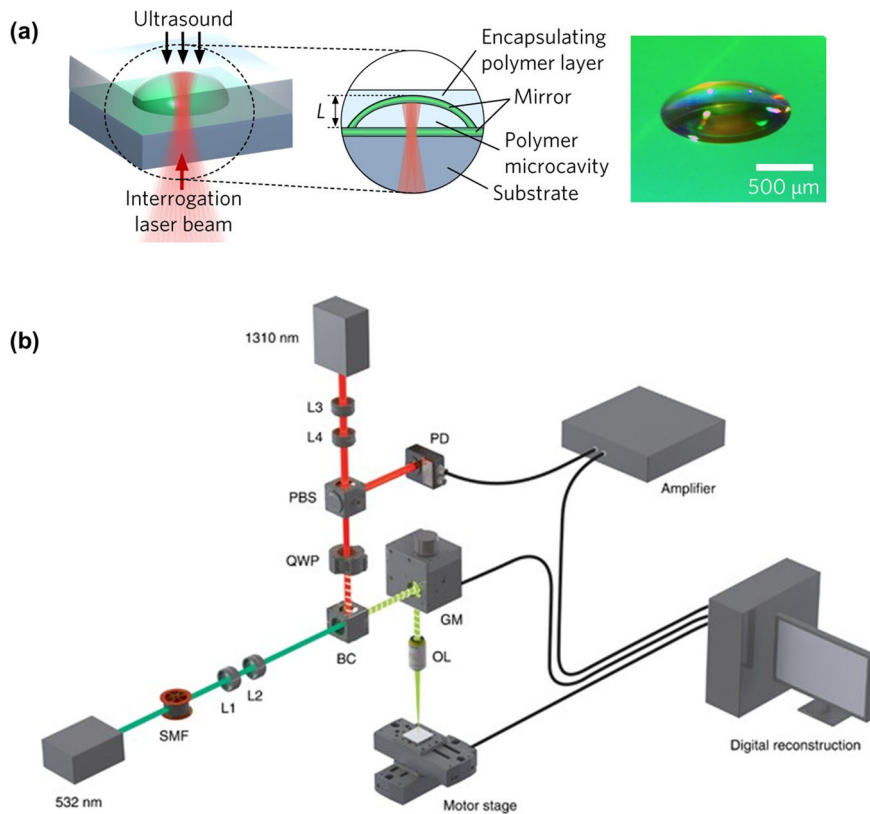
miniature fiber-optic ultrasound sensors featuring interferometric polymer optical cavities (Fig. 3a). By optimizing the fiber tip and cavity geometry, especially using a rounded tip and a plano-convex cavity, these optical sensors achieve near omnidirectional frequency response up to 80 MHz and a noise-equivalent pressure of 40 Pa. To apply their sensors to high-speed PAM, the group further combined this stationary fiber-optic ultrasound sensor with a custom-built fiber laser operating at a PRF of 2 MHz. They successfully imaged a $10 \times 10 \text{ mm}^2$ area in just 8 s, acquiring 16 million A-lines⁴⁷. Another all-optical detection method is photoacoustic remote sensing. This method can be used without the need for water coupling with the target, which can be particularly beneficial in applications involving electrical components or biological samples that cannot be immersed in water. In the remote sensing setup, Hajireza et al.⁵¹ developed a non-interferometric PAM system that uses a low-coherence probe beam aligned with the photoacoustic excitation beam for optimal detection of probe beam reflection (Fig. 3b). The system achieved high-speed imaging with galvanometer scanning of both laser beams. They imaged the capillary beds on a mouse ear at a C-scan rate of 30 Hz, but the FOV was limited to 50 μm .

Multiple excitation laser beams with a single-element ultrasound detector

One of the major utilities of PAM is functional imaging, such as measuring total hemoglobin concentration, hemoglobin oxygen saturation, oxygen metabolism, or blood flow. Functional PAM is based on analyzing PA signals generated from multiple laser wavelengths^{31,52}. Although many fast diode-pumped lasers have been successfully implemented to achieve high-speed PAM, they are generally limited in single wavelengths. Thus, multiple-wavelength laser technologies for high-speed functional PAM are needed. One example is a supercontinuum (SC) source^{47,53–57} coupled into a highly nonlinear fiber. The SC source, which has the advantage of wavelength tunability, was first applied to PAM by Billeh et al. in 2010⁵³. They used a laser with a PRF of 6.6 kHz and a wavelength tuning region of 600–1700 nm, demonstrating multispectral PAM with slow imaging speed. Chang et al. implemented a real-time imaging system, which acquired multispectral PAM and OCT images simultaneously⁵⁶. They achieved in-vivo imaging of mouse ears with a laser PRF of 1 MHz. While SC light sources provide multispectral PA imaging by filtering the light into discrete wavelength bands, the optical energy per band is low (tens of nanojoules), which limits the SNR of the images and the quantitative accuracy.

To overcome the relatively low energy of the SC light sources, stimulated Raman scattering (SRS) light sources have become popular in multispectral high-speed PAM. The SRS sources generate a few discrete spectral bands with high energy. Koeplinger et al.⁵⁸ first applied an SRS light source to PAM in 2011. They used a 6-m polarization-maintaining fiber and an Nd:YAG microchip laser with a 7.5 kHz PRF to generate four wavelengths with a pulse energy of $>80 \text{ nJ}$. Parsin et al.⁵⁹ first reported in-vivo functional PAM using an SRS light source. They expanded the output wavelengths to the near-infrared range, increased energy per band, and narrowed the peak spectra. Liang et al.⁶⁰ further developed an SRS-based multi-wavelength (532 nm, 545 nm, and 558 nm) pulsed laser with wavelength switching time of 220 ns. The multiple laser beams were combined and coupled into an optical fiber for photoacoustic excitation with 2 million pulses per second. As a follow-up study, combined with a polygon-scanning probe, they achieved a volumetric imaging rate of $\sim 1 \text{ Hz}$ over a $12 \times 5 \text{ mm}^2$ scanning area⁶¹. To further extend the functional imaging capabilities, they presented five-wavelength OR-PAM (Fig. 4a) for simultaneous imaging of hemoglobin concentration, oxygen saturation, blood flow speed, and lymphatic vessels. The five wavelengths (532, 545, 558, 570, and 620/640 nm) were temporally separated by several hundreds of nanoseconds by varying the delaying fiber lengths⁶². Similarly, Zhu et al.⁶³ used SRS-based dual-wavelength excitation with a water-immersible polygon-scanner (Fig. 4b) and achieved a volumetric functional imaging rate of 2 Hz over an FOV of $11 \times 7.5 \times 1.5 \text{ mm}^3$ with a spatial resolution of $\sim 10 \mu\text{m}$. The maximum B-scan frame rate is more than 2 kHz over a 11 mm scanning range.

Fig. 3 | Two representative high-speed PAM with optical detectors. **a** Schematic of plano-concave optical microresonator ultrasound sensor (L = cavity thickness) (shown on the left). The sensor comprises a plano-concave polymer microcavity encapsulated by a polymer layer. Photograph of the polymer microcavity without the encapsulating polymer layer is shown on the right (adapted with permission from ref. 50). **b** Remote sensing PAM with the 532 nm excitation beam and the 1310 nm probe beam. BC beam combiner; GM galvanometer mirror; L lens; OL objective lens; PBS polarized beam splitter; PD photodiode; QWP quarter-wave plate; SMF single mode fiber. (adapted with permission from ref. 51).



In a different approach, rather than using multiple wavelengths for functional imaging, Yao et al.³¹ applied a single-wavelength pulse-width-based method to perform high-speed imaging of the oxygen saturation of hemoglobin (sO_2). When first excited by a picosecond pulse and subsequently by a nanosecond pulse of the same wavelength and pulse energy, oxygenated hemoglobin (HbO_2) and deoxygenated hemoglobin (HbR) present different optical absorption saturation levels. From PA signals acquired with the two laser pulses, the relative concentrations of HbO_2 and HbR can be quantified, and thus sO_2 can be computed. One important advantage of this method is that it does not suffer from wavelength-dependent optical attenuation as the traditional multi-wavelength method.

Multiple laser beams with parallel ultrasound detection

Instead of the point-by-point detection in PAM, acquiring ultrasound data in parallel with wide-field illumination is an effective strategy to accelerate the speed. This approach overcomes the limited laser PRF in point-by-point scanning and thus potentially the spatial undersampling. In PAM systems utilizing multiple laser beams and parallel ultrasound detection, the excitation laser beam is shaped into a grid of focused spots on the sample surface through techniques such as beam shaping (e.g., using a microlens array)^{64–67} or beam splitting (e.g., using a beam splitter)⁶⁸. The generated PA signals are then detected by a ultrasound transducer array with multiple elements. This configuration allows for simultaneous acquisition of ultrasound signals at multiple locations, enhancing the imaging speed.

Chen et al.⁶⁸ first introduced multifocal structured-illumination PAM via beam splitting (Fig. 5a). They shaped the excitation laser beam into a grid of focused spots on the tissue surface using a beam-splitting diffraction grating. This system provided a 15 Hz C-scan frame rate over a 10 mm FOV, with a spatial resolution of 28 μ m. Xia et al.⁶⁶ developed a 2D multifocal optical-resolution photoacoustic-computed microscopy system, utilizing a 2D microlens array for beam shaping and a full-ring ultrasonic transducer array for signal detection. The 10 \times 10 mm² microlens array created 1800 optical foci within the focal plane of the ring transducer array. This setup needed 36 s to image a 10 \times 10 mm² FOV. Li et al.⁶⁹ developed photoacoustic

topography through an ergodic relay (PATER), using a single-element ultrasonic transducer. This system used an ergodic relay (ER) to encode spatial information into temporal signatures of the acoustic signals detected by the transducer, enabling parallel detection of photoacoustic signals with a single laser shot. PATER achieved a high frame rate of up to 2 kHz with an FOV of up to 8 \times 6 mm² and a lateral resolution of 110 μ m. They further combined the ER with a 2D microlens array to achieve high-speed PAM⁷⁰ (Fig. 5b). This system efficiently captured photoacoustic signals from 400 optical foci in parallel, enabling rapid image formation through raster scanning of the optical foci. This setup provided a 10 \times 10 mm² FOV with an imaging time of less than 10 s and a lateral resolution of 13 μ m.

Deep learning methods for high-speed PAM

In high-speed PAM, achieving high spatial resolution across a large field of view traditionally requires scanning that adheres to the Nyquist-Shannon sampling theorem. This theorem mandates that the scanning step size should be no more than half of the desired spatial resolution (e.g., 5 μ m) to accurately capture fine details such as microvessels, which often have diameters of at least 10 μ m²⁴. However, this dense spatial sampling inherently slows down imaging speeds. Recent advancements in fast-scanning technologies, including Galvo mirrors, microelectromechanical mirrors, and polygon scanners, have significantly enhanced scanning speeds. Despite these technological improvements, the overall imaging speed is frequently limited by the laser's pulse repetition rate and the safety constraints associated with laser use⁵³. To address this, increasing the scanning step size or employing sparse sampling has become a common, though imperfect solution, as it often results in degraded image quality, including reduced resolution and spatial aliasing. Given the limitations of hardware improvements in resolving undersampling issues, recent research has increasingly turned to deep learning (DL) techniques to enhance high-speed PAM. Building on the success of DL in photoacoustic computed tomography (PACT)—where it has been used for artifact removal, target identification, and improving sparse sampling^{71–74}, DL has shown considerable promise in addressing the challenges posed by undersampling in high-speed

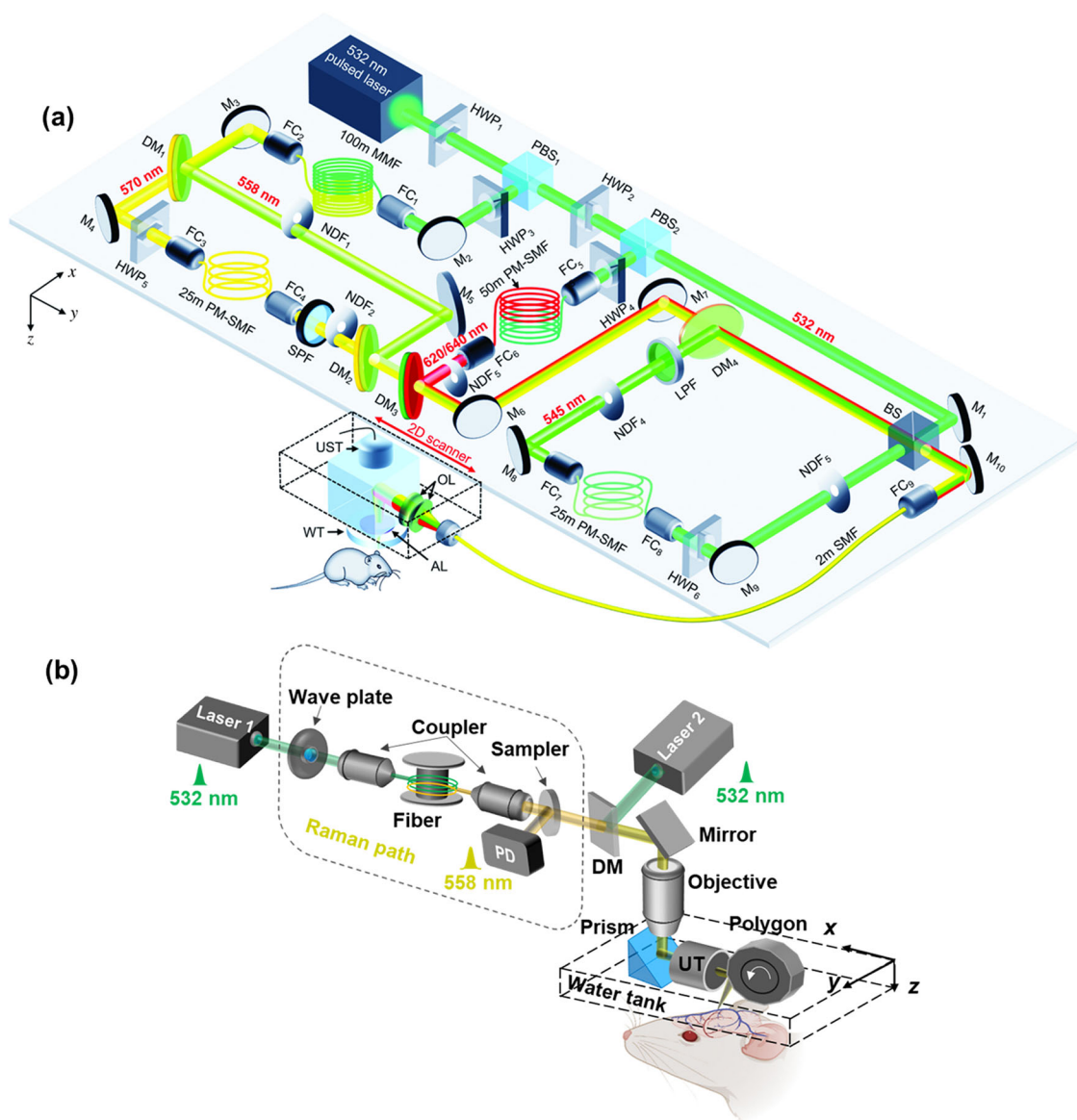


Fig. 4 | High-speed PAM based on multiple laser beams with a single-element ultrasound detector. **a** Schematic of five-wavelength OR-PAM. AL, acoustic lens; BS, beam splitter; R/T, 10/90; DM 1, DM 2, 565-nm long-pass dichroic mirror; DM 3, 600 nm short-pass dichroic mirror; DM 4, 550-nm long-pass dichroic mirror; FC, fiber coupler; HWP 1–6, half-wave plate; LPF, 537-nm long-pass filter; M 1–10, mirror; MMF, graded-index multimode fiber; NDF 1–5, neutral density filter; OL, optical lens; PBS 1–2, polarizing beam splitter; PM-SMF, polarization-maintaining

single-mode fiber; SPF, 580 nm short-pass filter; UST, ultrasonic transducer; WT, water tank. (adapted with permission from ref. 62). **b** Schematic of the two-wavelength high-speed PAM system with a polygon scanner. The 532 nm light path and the 558 nm Raman path are combined for functional imaging. DM dichroic mirror; PD photodiode; UT ultrasound transducer. (adapted with permission from ref. 63).

PAM^{75–78}. These DL approaches offer innovative solutions to maintain high image quality and resolution, even when constrained by the physical limitations of hardware.

Vu et al.⁷⁵ introduced an innovative deep image prior (DIP) approach to enhance the quality of undersampled PAM images, aiming to boost the imaging speed of fast PAM systems (Fig. 6a). Unlike conventional deep learning methods, their DIP model does not require pre-training or fully-sampled ground truth images, making it adaptable and efficient for various imaging targets. The model works by iteratively seeking an optimized, fully sampled image that approximates the undersampled image, using a known downsampling mask. This technique has demonstrated significant improvements in image quality, even when utilizing as few as 1.4% of the fully sampled pixels. The method has been successfully tested on mouse brain vasculature images, showing promising results in both phantoms and *in vivo* studies.

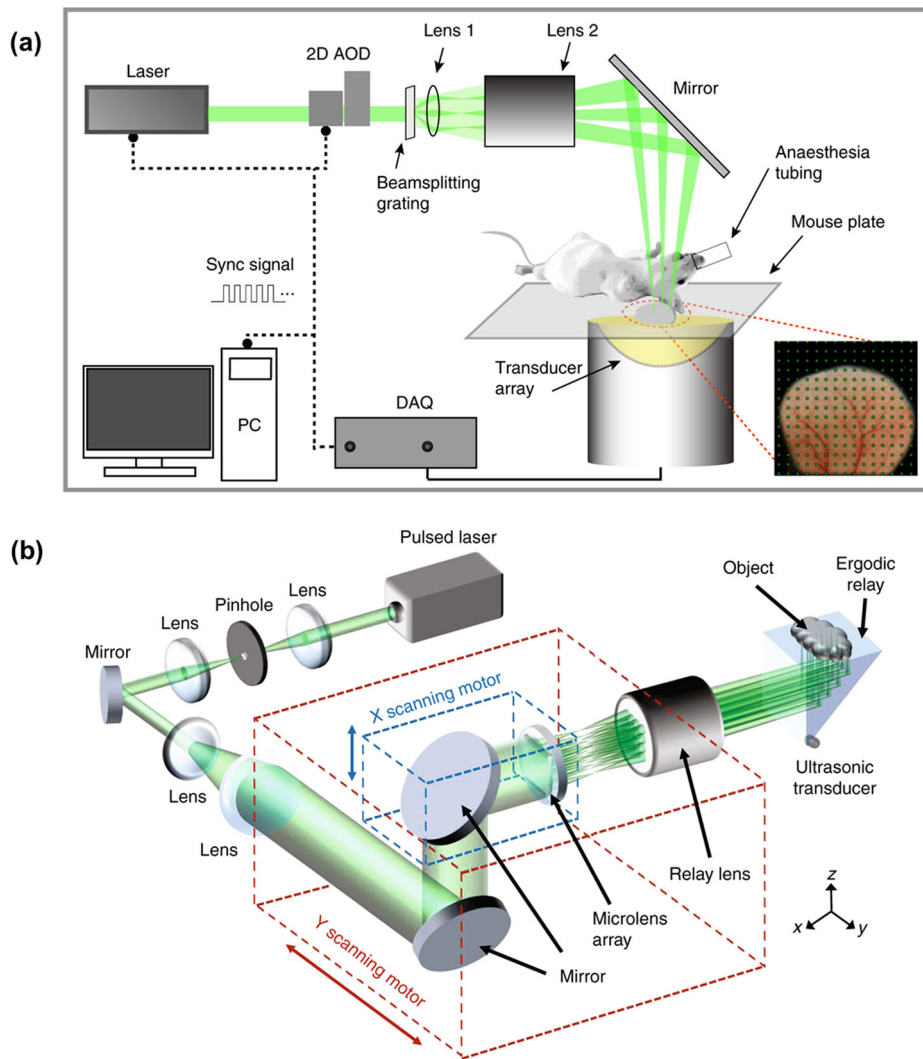
Seong et al.⁷⁸ developed a deep learning-based method for fully reconstructing undersampled 3D PAM data, significantly enhancing imaging speed and reducing data size (Fig. 6b). By modifying the super-resolution ResNet (SRRResNet) to accommodate flexible upscale ratios along single- and dual-axes, their approach allows for robust reconstruction across various undersampling ratios, outperforming traditional interpolation-based methods. The proposed model demonstrated an 80-fold increase in imaging speed and an 800-fold reduction in data size. The proposed method has been demonstrated under various experimental conditions, effectively shortening imaging time while significantly reducing the data size.

Preclinical and clinical applications

As highlighted in several comprehensive review articles^{9,14,79–84}, PAM has garnered interest in both fundamental research and clinical applications due to its superior resolution, balanced imaging depth, and enhanced contrast

Fig. 5 | High-speed PAM based with multiple laser beams and parallel ultrasound detection.

A Multifocal structured-illumination PAM with grating-based beam splitting (adapted with permission from ref. 68). **b** System schematic of multifocal PAM with ergodic relay. The focus plane of the microlens array is imaged onto the surface of the ER prism to illuminate the object. A single-element ultrasonic transducer is attached to a corner of the ER to detect the encoded PA signals (adapted with permission from ref. 70).



compared to traditional optical methods. Despite its extensive applications, traditional PAM systems have relatively low imaging speeds, which have restricted their ability to capture dynamic biological processes such as rapid drug responses and neural activities. Thus, accelerating imaging speed is an active research focus over the past decade, with the aim of unlocking more biomedical applications for PAM. These efforts have successfully improved PAM performance for capturing dynamic functions in both small animal models and humans. This section highlights PAM's rapidly expanding biomedical applications, including brain imaging, pregnancy monitoring, dermatology, histology, and detecting circulating cells.

Brain imaging

The hyperemic response of neuronal vasculature has been widely used to study neural activities^{85–87}. However, this response spreads quickly from the origin of neural activity, which demands high imaging speed for high-fidelity research. High-speed PAM has emerged as a powerful solution to address these challenges by allowing real-time visualization of microvascular morphology and blood oxygenation. This technique provides a precise view of brain functions, opening new avenues for investigating fast physiological processes in the brain^{31,63,87–91}.

In 2015, Yao et al.³¹ developed the high-speed PAM system based on the water-immersible MEMS-scanner, which was capable of high-resolution imaging of the mouse brain through an intact skull. They visualized the mouse brain's hyperemic response to electrical stimulation of the hindlimbs. The results show increased blood perfusion (Fig. 7a) and

artery dilation in the contralateral somatosensory region during stimulation, along with a rise in oxygen saturation levels in the veins and deep capillary beds. He et al.⁹⁰ further contributed to the study by imaging single-impulse-stimulated hemodynamics. They captured a transient initial dip in sO_2 across different microvascular compartments and revealed that this initial dip begins as early as 0.13 s after stimulus onset (Fig. 7b). This work provided valuable insights into the initial dip phenomenon. These findings illustrate the potential of high-speed PAM in future applications such as brain-computer interfaces.

In 2022, using the polygon-scanner-based high-speed PAM, Zhu et al.⁶³ conducted proof-of-concept studies on the mouse brains under various pathological and physiological conditions, including systemic hypoxia, sodium nitroprusside, and stroke. For the first time, with a whole-brain FOV and micro-vessel resolution, they simultaneously captured vasoconstriction and hypoxia as a result of spreading depolarization (SD) waves—the intense neuronal and glial depolarization waves propagating at millimeters per minute (Fig. 7c). They showed that prolonged cerebral ischemia could trigger SD waves, indicated by the microvascular constriction and increased oxygen extraction. The system's high resolution, extensive FOV, and high imaging speed facilitated monitoring of SD wave local initiation and tracking of its propagation and vasoconstriction across the cortex. This study showed the great potential of high-speed PAM for identifying stroke cores and penumbra in real-time, evaluating their expansion, and assessing neuroprotective therapies in future studies.

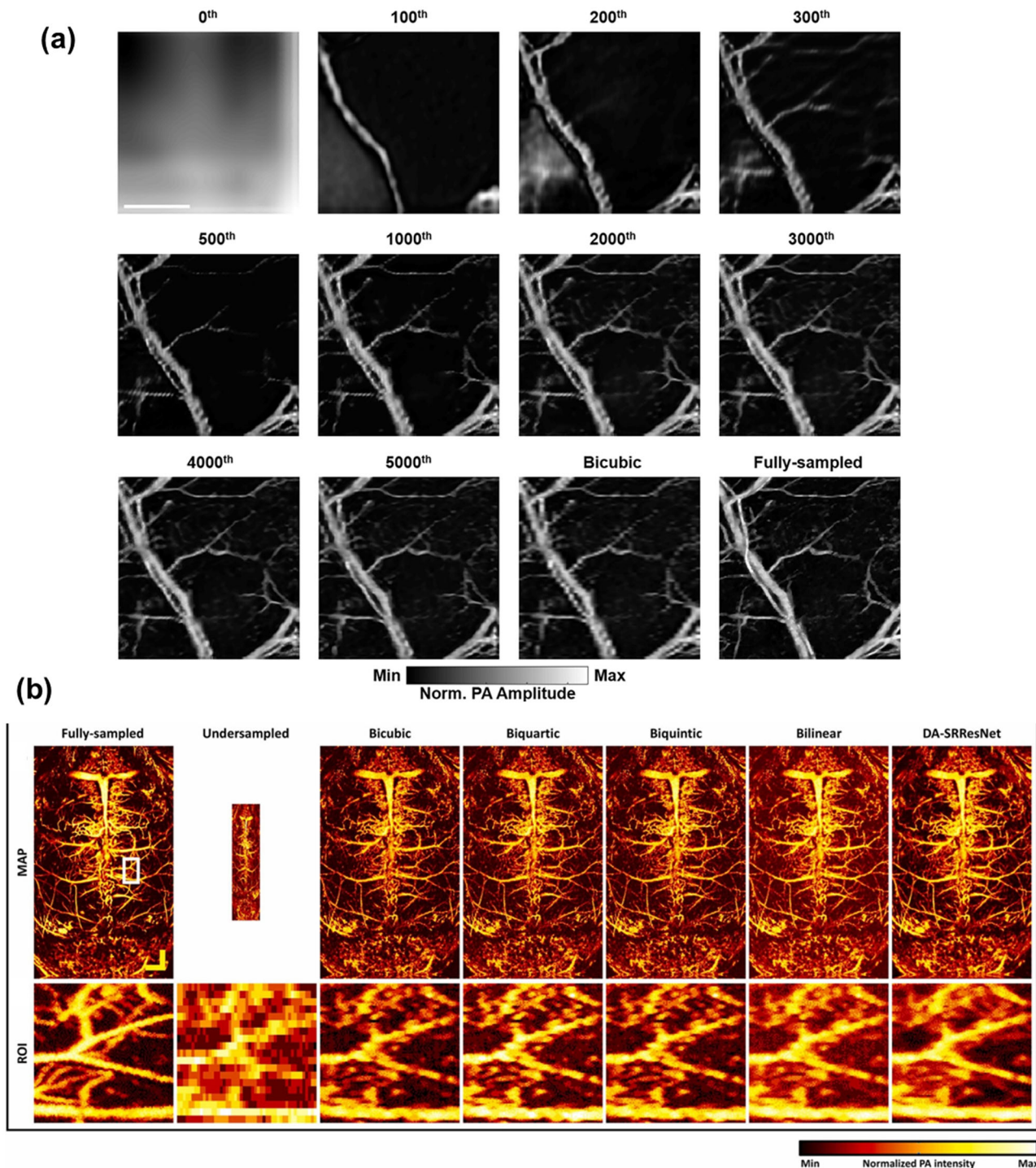


Fig. 6 | Deep Learning methods for high-Speed PAM. **a** Evolution of the DIP optimization process at incrementing iterations. The image of mouse brain vasculature is undersampled. The bicubic interpolation and fully-sampled image are also presented. Scale bar: 0.5 mm (adapted with permission from ref. 75).

b Representative reconstructed PAM images of mouse brain vasculature by different methods, and close-up images of ROI (indicated by the white box). Scale bar: 1 mm (adapted with permission from ref. 78).

Pregnancy monitoring

PAM has been used in the field of pregnancy studies^{32,66,92–94}, offering unique insights into the anatomy and physiology of pregnancy, particularly in monitoring and assessing placental, fetal, and uterus health. Recently, Zhu et al.³² advanced the study of placental development throughout the mouse pregnancy using a newly developed implantable placenta window combined with ultrafast functional PAM. This setup provided detailed spatiotemporal imaging and allowed for longitudinal investigation into the placenta's response to various

conditions. Healthy pregnancies showed a rise in sO_2 levels until mid-gestation, followed by a decrease—early increases aiding embryonic development and later decreases preparing for birth (Fig. 8a). The authors also observed adverse effects from chronic alcohol consumption, which increased placental blood flow and oxygenation, potentially harming the developing fetus with excessive oxygen stress. Additionally, the study investigated the impacts of cardiac arrest (CA) and inflammation during pregnancy and observed harmful changes in placental blood flow and microvessel density as a result of these deadly

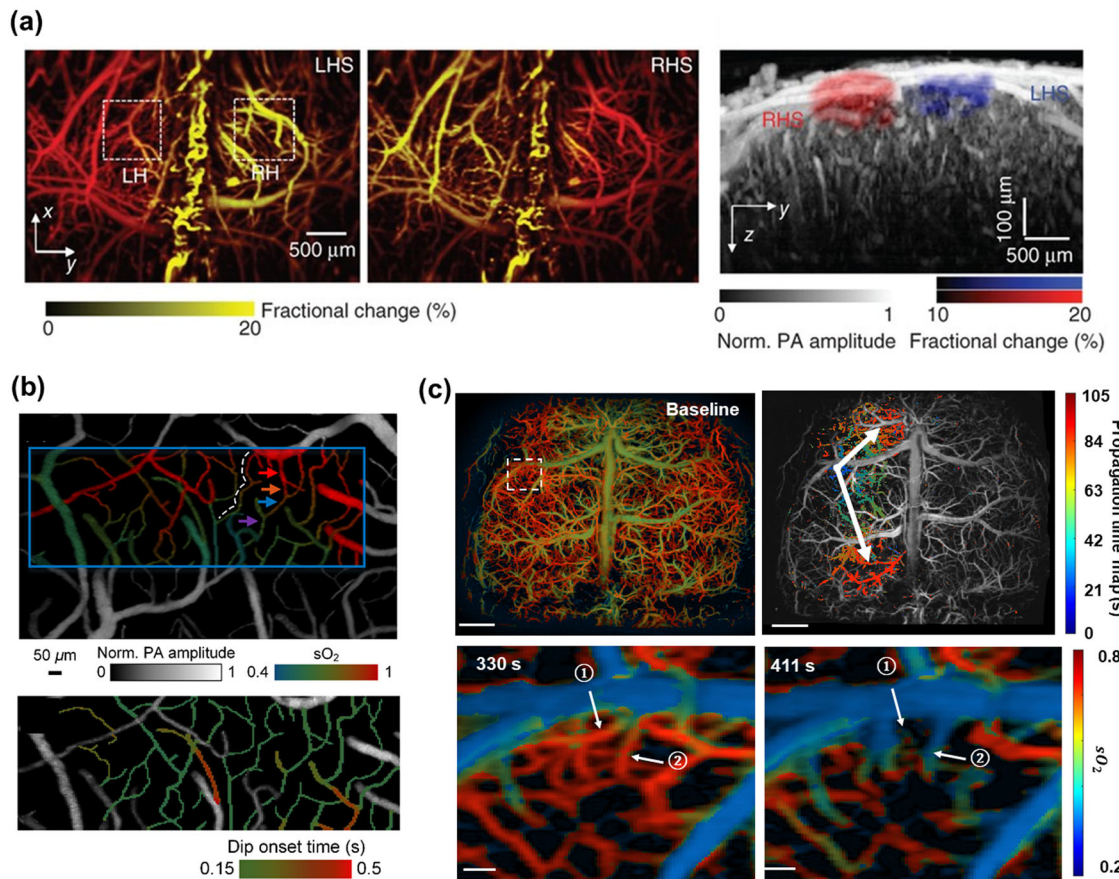


Fig. 7 | High-speed PAM of the mouse brain. **a** High-speed PAM of mouse brain responses to electrical stimulations of the hindlimbs of mice. (Left) Fractional PA signal amplitude changes (shown in yellow) in response to left hindlimb stimulation (LHS) and right hindlimb stimulation (RHS), superimposed on the vascular image (shown in red). LH, left hemisphere; RH, right hemisphere. (Right) Depth-resolved photoacoustic amplitude (PA) responses showing a coronal section of the brain. The responding areas in the LH and RH are shown in red and blue, respectively, and superimposed on the grayscale coronal projection image. The signal amplitude in the coronal projection image was normalized depth-wise (adapted with permission from ref. 31). **b** Brain vasculature oxygenation responses to electrical stimulations. (Top) sO₂ mapping of the somatosensory area. The blue rectangle illustrates the region of interest for the subsequent functional imaging studies. (Bottom) Timing of the initial dip onset, superimposed onto the grayscale structure image (adapted with permission from ref. 90). **c** Brain images of the stroke-induced SD waves. (Top) A sO₂ image of the whole cortex at baseline and propagation time map of a representative SD wave. Arrows represent the direction of SD wave. (Bottom) Close-up sO₂ images of the SD wave origin at two different time points, as indicated by the white dotted rectangle in the baseline image (adapted with permission from ref. 63).

from ref. 31). **b** Brain vasculature oxygenation responses to electrical stimulations. (Top) sO₂ mapping of the somatosensory area. The blue rectangle illustrates the region of interest for the subsequent functional imaging studies. (Bottom) Timing of the initial dip onset, superimposed onto the grayscale structure image (adapted with permission from ref. 90). **c** Brain images of the stroke-induced SD waves. (Top) A sO₂ image of the whole cortex at baseline and propagation time map of a representative SD wave. Arrows represent the direction of SD wave. (Bottom) Close-up sO₂ images of the SD wave origin at two different time points, as indicated by the white dotted rectangle in the baseline image (adapted with permission from ref. 63).

conditions. Qu et al.⁹³ developed a transvaginal fast-scanning optical-resolution photoacoustic endoscope, achieving high-resolution in-vivo imaging of the vascular network in the human cervix (Fig. 8b). This technology surpasses current clinical methods, such as colposcopy, transvaginal ultrasound and MRI, in terms of spatial resolution and contrast. They illustrated the morphological differences in the vasculature of the human ectocervix, uterine body, and sublingual mucosa, and also demonstrated the longitudinal variations in the cervical vasculature of pregnant women. This advancement holds significant potential for screening visceral pathological changes associated with pregnancy angiogenesis. Rao et al.⁹⁴ utilized high-speed OR-PAM to examine microvascular characteristics in ovarian and fallopian tube tissues (Fig. 8c). By analyzing excised post-surgery human specimens, quantitative parameters such as three-dimensional vascular segment count, volume, and length were extracted. The study revealed that malignant tissues exhibited larger, more tortuous vessels, and a greater number of smaller vessels of varying sizes. In contrast, benign and normal tissues presented uniformly sized small vessels. PAM offers a rapid assessment tool that could potentially reduce unnecessary surgeries by aiding preoperative and intraoperative decision-making, especially in minimally invasive procedures.

Dermatology

Skin vascular abnormalities are critical indicators for various skin diseases, reflecting tissue health and presenting distinct patterns associated with

disease progression. Traditional clinical methods, such as histopathology and dermoscopy, while considered as the gold standard for diagnosis⁹⁵, lack the ability to render 3D vascular images of the skin. Noninvasive and precise imaging of the skin's vascular network could provide crucial information for diagnosing and assessing dermatological conditions. High-speed PAM offers a promising alternative for clinical dermatological applications^{96–100}. In 2017, Aguirre et al.⁹⁶ presented raster-scan photoacoustic mesoscopy. This system used ultra-broadband (10–180 MHz) ultrasound detection that balanced the imaging depth, resolution, and contrast for clinical dermatology. The handheld device allowed for detailed visualization of skin vessel morphology in the dermis and sub-dermis of psoriasis patients (Fig. 9a), enabling the quantification of inflammation and other psoriasis biomarkers without contrast agents or invasive procedures. The PAM biomarkers correlated well with clinical scores, highlighting the potential of PAM to offer new insights into disease progression and treatment monitoring of inflammatory skin conditions. High-speed PAM has also shown promise in clinical skin cancer detection. Xu et al.¹⁰⁰ utilized PAM for in-vivo imaging of a subcutaneously inoculated B-16 melanoma in a mouse (Fig. 9b). PAM successfully resolved the blood vasculature surrounding the melanoma and was able to visualize the tumor's boundaries up to a depth of 1.6 mm. High-resolution and high-speed PAM has further proven effective in imaging and analyzing microvascular dynamics in human extremities, particularly in fingers^{101,102}. By utilizing a dual-wavelength PAM system, Ahn et al.¹⁰²

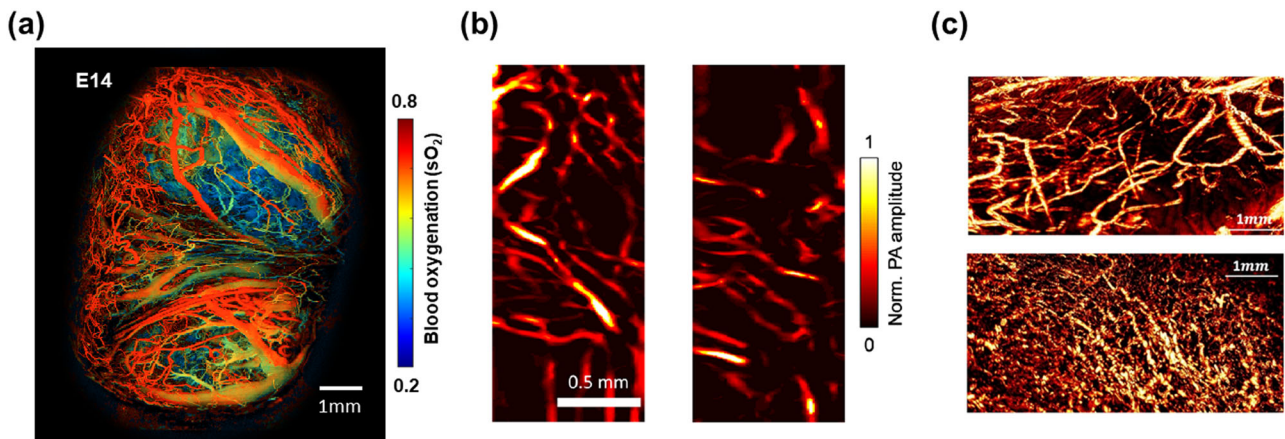


Fig. 8 | High-speed PAM of pregnancy. **a** The vessel-by-vessel sO₂ mapping of a healthy mouse placenta at E14 by high-speed PAM. A total of three placentas were observed simultaneously via the placental window (adapted with permission from ref. 32). **b** In-vivo PAM images of the anterior surface of the ectocervix acquired from a pregnant woman at 32 (left) and 36 (right) weeks of gestation (adapted with

permission from ref. 93). **c** A high-speed PAM image of blood vessels of a normal ovary from a 59-year-old post-menopausal woman (top) and a normal fallopian tube from a 57-year-old post-menopausal woman (bottom) (adapted with permission from ref. 94).

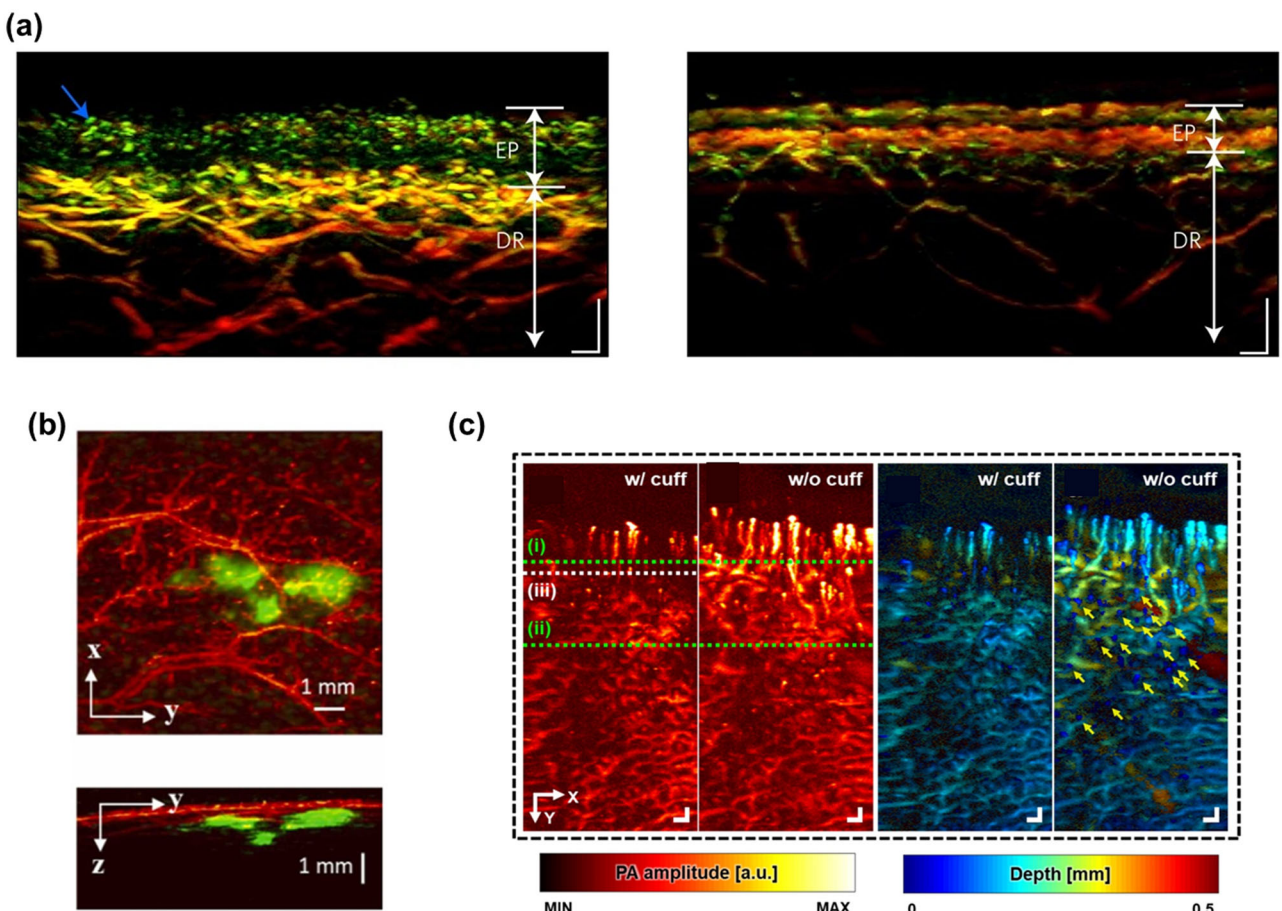


Fig. 9 | High speed PAM in dermatology. **a** PAM images of healthy skin (right) versus adjacent psoriatic skin (left). The psoriatic skin image shows the top part of elongated capillary loops (blue arrow) that almost climbed to the skin surface through elongated rete ridges. The capillaries appeared in green, interleaved with thickened epidermal (EP) structures as a result of acanthosis. These structures appeared in red with poor contrast due to loss of pigmentation. Below the epidermis, a dilated and dense vascular structure of the dermis (DR) is resolved (in red). Capillary loops were observed in green and separated from the epidermis (red) and

the dilated dermal vasculature (red). Scale bars, 200 μm. Adjacent healthy skin showed a layered EP with clearly resolved vessels in the DR. Scale bars, 200 μm (adapted with permission from ref. 96). **b** Top- (top) and side- (bottom) view PAM images of a subcutaneously inoculated B16-melanoma in a nude mouse (adapted with permission from ref. 100). **c** High-speed PAM of blood perfusion in a finger during brachial cuffing and after release along with corresponding depth-encoded images. All scale bars are 200 μm (adapted with permission from ref. 102).

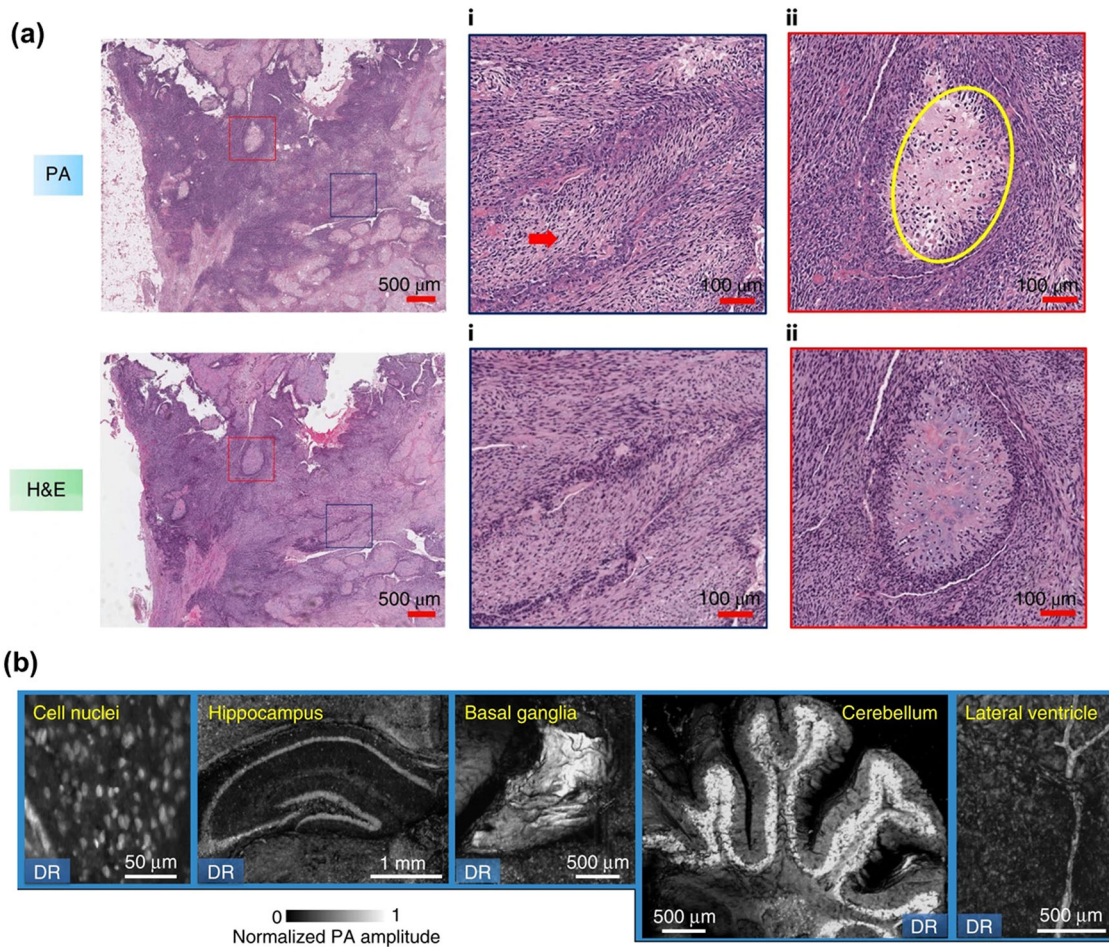


Fig. 10 | High-speed PAM for histology. **a** Label-free UV-PAM virtual histology of undecalcified bone via unsupervised deep learning (top) and the corresponding H&E histology images (bottom). Close-up images show neoplastic spindle cells (red arrows) arranged in vague streaming and fascicular patterns (i), and a nodule of neoplastic chondroid material (ii, yellow circle), with corresponding H&E histology

images. Scale bars, 500 μ m (a–d), 100 μ m (in all closed-up images) (adapted with permission from ref. 103). **b** Image gallery of an unstained mouse brain embedded in agarose blocks. All features are shown in coronal view, highlighting the absorption contrast by DNA/RNA (adapted with permission from ref. 110).

continuously imaged the cross-sectional plane of fingertips to monitor changes such as arterial pulsation, oxygen consumption during arterial occlusion, and subsequent blood perfusion (Fig. 9c). These parameters can be crucial clinical indicators for early detection, diagnosis, and prognosis of skin vascular diseases.

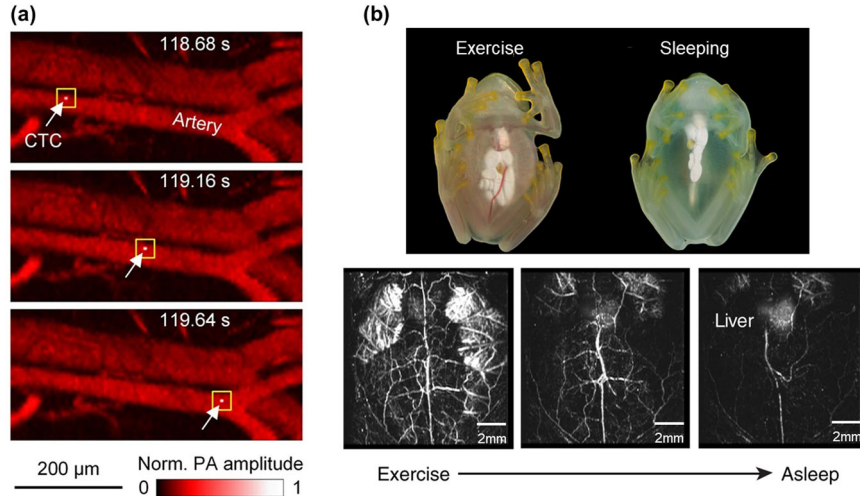
Histology

Surgical margin assessment (SMA) is crucial for reducing cancer recurrence, typically relying on postoperative histological analysis which can lead to re-excision surgeries that negatively impact quality of life. Intraoperative techniques such as frozen sectioning and imaging with ultraviolet surface excitation (MUSE) have been explored with limited success. Ultraviolet PAM (UV-PAM) has emerged as a promising alternative, providing rapid, label-free imaging of cell nuclei using DNA/RNA as the endogenous contrast^{67,103–109}. UV-PAM shows great potential for real-time SMA. Improving the imaging speed can further accelerate UV-PAM's clinical translation. Wong et al.¹⁰⁵ applied a UV-PAM system to image fixed, unprocessed breast tumors with high quality comparable to conventional histology. With the initial success, the authors improved the imaging speed by 40-fold by using a microlens array in conjunction with an ultrasonic transducer array⁶⁷. Shi et al.¹⁰⁴ further developed ultraviolet-localized mid-infrared (MIR) PAM (ULM-PAM), enabling high-resolution, MIR imaging of fresh biological samples, free of water background. ULM-PAM employed a pulsed MIR laser for thermal tagging and a confocal ultraviolet laser for photoacoustic detection. The ULM-PAM system offers superior resolution

and contrast over traditional MIR PAM by utilizing the shorter ultraviolet wavelength for detection. This approach enhances penetration into thicker samples, making ULM-PAM ideal for label-free histology and detailed imaging of structures like lipids and proteins in thick tissue slices. In 2023, Cao et al.¹⁰³ demonstrated a real-time 3D contour-scanning UV-PAM system to rapidly image rough surfaces of calcified bone tumors. This high-speed, label-free method allows for imaging thick, unprocessed bone with minimal preparation, offering a faster alternative to traditional, time-consuming pathological techniques. This label-free UV-PAM technique was validated by standard hematoxylin-and-eosin (H&E) histology. UV-PAM also enables pathologists to identify cancerous features effectively through virtual staining facilitated by an unsupervised generative adversarial network (Fig. 10a). In addition to bone, this method could potentially provide rapid pathological examination and intraoperative decision-making for various tissue types. In a similar approach, Wong et al.¹¹⁰ presented the microtomy-assisted PAM (mPAM) technique, which enables three-dimensional imaging of whole organs, such as mouse brains, without the need for tissue staining or sectioning. The system offers real-time display of cross-sectional images during data acquisition, providing high-resolution, label-free imaging of cell nuclei (Fig. 10b), blood vessels, and other anatomical structures using endogenous contrasts. This technique, which employs ultraviolet light and dual-wavelength illumination, provides histology-like imaging and deeper tissue analysis, offering a viable alternative to traditional histological methods. Although the scanning process is currently time-consuming, ongoing advancements, such as faster lasers and

Fig. 11 | High-speed PAM for sensing circulating cells.

a Fused PA flowcytometry image at 532 nm and 1064 nm, showing single CTCs traveling in the vasculature, with the white arrow and yellow box indicating the detected CTC. Three snapshots show a single CTC traveling in the artery, with times labeled relative to CTC injection (adapted with permission from ref. 114). **b** Flash photography illustrates the visible change in RBC perfusion of active and sleeping glassfrogs (top). High-speed PAM images show the dynamics of RBC perfusion (adapted with permission from ref. 117).



improved scanning mechanisms, hold the potential to revolutionize whole-organ microscopy.

Circulating cells

Current clinical methods for detecting circulating tumor cells (CTCs) face challenges in sensitivity and throughput, limited by the small volume of blood samples and the requirement for biomarker labeling. Photoacoustic imaging offers a label-free alternative by exploiting the natural melanosome absorption contrast of melanoma cells in the near-infrared spectrum^{111–116}. Moreover, Galanzha et al.¹¹³ developed a dual-targeted approach that combines magnetic and photoacoustic flow cytometry to detect CTCs in the bloodstream of tumor-bearing mice. Their innovative method employed magnetic nanoparticles to target receptors specific to breast cancer cells and gold-plated carbon nanotubes conjugated with folic acid to boost PA contrast. The unique combination of nanoparticles with distinct magnetic and optical properties improved both the specificity and sensitivity of CTC detection. This method achieved precise detection of even low counts of CTCs. They further developed an in-vivo photoacoustic flow cytometry platform for the label-free detection of melanin-bearing CTCs in melanoma patients¹¹². This method, capable of detecting individual CTCs down to a sensitivity of 1 CTC per liter of blood, significantly surpassed traditional assays by about 1000 times. It offered a noninvasive, real-time blood test conducted directly in the patient's bloodstream, achieving results in seconds and enabling the detection of CTC clusters and CTC-clot emboli. The photoacoustic flow cytometry (PAFC) system's effectiveness was demonstrated by detecting CTCs in 96% of melanoma patients. This approach can also facilitate the real-time destruction of CTCs, thereby potentially preventing metastasis and enhancing patient prognosis. He et al.¹¹⁴ developed a dual-wavelength high-speed PAM that integrates a melanoma-specific, nanosecond-pulsed laser therapy mechanism, enabling the detection and immediate destruction of CTCs in the bloodstream. It offers high-resolution, in-vivo label-free imaging and the real-time eradication of single circulating melanoma cells in both arteries and veins of mice without harming surrounding tissues (Fig. 11a). In addition to imaging CTCs, high-speed PAM can be applied to imaging real-time perfusion of red blood cells (RBCs) in vivo. Taboada et al.¹¹⁷ utilized high-speed PAM to understand the physiological mechanisms of vertebrate transparency by imaging the circulation of RBCs in glassfrogs. Glassfrogs achieve remarkable transparency as a form of camouflage by actively regulating the density of their circulating RBCs, which are strong light-absorbing pigments in vertebrates. The PAM results reveal that during rest, glassfrogs increase their transparency by sequestering about 89% of their RBCs into their liver, thus reducing circulating RBCs and enhancing transparency by two- to three-fold (Fig. 11b). This biological adaptation is crucial not only for camouflage but also

provides insights into metabolic and hemodynamic functions, as well as potential strategies for preventing vascular pathologies such as thromboses, given their ability to pack and unpack large volumes of RBCs daily without clotting.

Conclusions

This review has introduced the technical advancements and applications of high-speed PAM, highlighting its transformative potential in observing dynamic biological processes at unprecedented spatial and temporal resolution. High-speed PAM stands out by enabling label-free real-time visualization of morphological and functional changes within living tissues, thereby enhancing our understanding of complex biological systems such as brain activities, placenta development, and glassfrog transparency. This capability is important in developing innovative diagnostic and therapeutic strategies, particularly beneficial in oncology, cardiology, and neurology.

Despite these advancements, the journey of high-speed PAM is far from complete. The field is filled with numerous opportunities and challenges that continue to advance both scientific research and clinical applications. 1) Artificial intelligence (AI) can potentially be used to enhance high-speed PAM image quality^{63,75} and interpretability¹⁰³. By deconstructing photoacoustic images into meaningful phenotypic descriptors, AI can help translate complex imaging data into clinically useful information, thus improving both the utility and application of PA imaging in clinical settings. 2) In the past decade, optical ultrasound detection methods have advanced significantly^{20,50,51,118–122}, offering high sensitivity, smaller sensors, full transparency, broader frequency response, improved axial resolution, and contact-free measurement. These enhancements expand the applicability of PAM in biomedical and clinical settings, presenting new opportunities for integration into point-of-care healthcare technologies. 3) Making high-speed PAM systems portable and cost-effective remains crucial for their widespread adoption in clinical environments. Efforts to develop handheld, economical PAM systems are ongoing^{28,96,123,124} and are expected to transform the accessibility of this technology in healthcare settings. 4) Integrating PAM with other modalities, such as ultrasound, OCT, or fluorescence microscopy, is crucial for contemporary clinical needs^{21,125–129}. This integration facilitates the seamless adoption of PAM into clinical workflows and potentially broadens the spectrum of its applications. By combining the unique advantages of each imaging technology, the multimodal systems can offer more comprehensive diagnosis than each single modality alone.

Additionally, the imaging depth of OR-PAM restricts its potential in preclinical and clinical settings. Although OR-PAM has the advantage of only one-way optical propagation, which allows for slightly deeper imaging compared to traditional optical imaging, it is still generally limited to imaging one optical transport mean free path in tissue (~1 mm). Like two-

photon microscopy, imaging using longer wavelengths allows for increased penetration depth due to decreased optical attenuation¹³⁰. However, using only near-infrared wavelengths also severely limits the potential sources of imaging contrast. Improving the sensitivity of ultrasound detection also allows for increased penetration depth. This can be achieved through broadband and low-noise ultrasonic detectors, such as optical ultrasound detectors. Additionally, innovative solutions for focusing light deeper in scattering media have been explored in photoacoustics, including wavefront engineering¹³¹ and acoustic waveguides¹³². These methods can extend imaging depths in tissues while maintaining optical resolution, however, at the expense of system complexity and/or imaging speeds. Achieving deeper imaging while maintaining high speed and resolution will be crucial for OR-PAM to see increased applications in research and healthcare settings.

In conclusion, high-speed PAM has achieved notable advances for both basic research and clinical applications, offering unique imaging contrasts and exceptional spatiotemporal resolution. The integration of PAM into clinical workflows is poised to significantly enhance disease diagnosis, treatment monitoring, and biomedical research. However, the full potential of high-speed PAM can only be realized through overcoming remaining technical challenges and fostering collaborative development efforts among academia, industry, and healthcare practitioners. These collaborations are vital for transitioning PAM from a research tool to routine clinical equipment. Future progress will depend on continuous technological innovation and sustained interdisciplinary efforts.

Data availability

No datasets were generated or analysed during the current study.

Received: 23 June 2024; Accepted: 17 October 2024;

Published online: 06 November 2024

References

1. Bell, A. G. The photophone. *Science* **os-1**, 130–134 (1880).
2. Manohar, S. & Razansky, D. Photoacoustics: a historical review. *Adv. Opt. Photonics* **8**, 586–617 (2016).
3. Bell, A. G. On the production and reproduction of sound by light. *Am. J. Sci.* **3**, 305–324 (1880).
4. Vengerov, M. An optical-acoustic method of gas analysis. *Nature* **158**, 28–29 (1946).
5. Rosencwaig, A. Photoacoustic spectroscopy of biological materials. *Science* **181**, 657–658 (1973).
6. Thomas, R. et al. Subsurface flaw detection in metals by photoacoustic microscopy. *J. Appl. Phys.* **51**, 1152–1156 (1980).
7. Oraevsky, A. A., et al. Laser-based optoacoustic imaging in biological tissues. in *Laser-Tissue Interaction V; and Ultraviolet Radiation Hazards*. (SPIE, 1994).
8. Wang, L. V. Multiscale photoacoustic microscopy and computed tomography. *Nat. Photonics* **3**, 503–509 (2009).
9. Wang, L. V. & Yao, J. A practical guide to photoacoustic tomography in the life sciences. *Nat. Methods* **13**, 627–638 (2016).
10. Lin, L. & Wang, L. V. The emerging role of photoacoustic imaging in clinical oncology. *Nat. Rev. Clin. Oncol.* **19**, 365–384 (2022).
11. Lin, L. et al. Photoacoustic computed tomography of breast cancer in response to neoadjuvant chemotherapy. *Adv. Sci.* **8**, 2003396 (2021).
12. Kothapalli, S.-R. et al. Simultaneous transrectal ultrasound and photoacoustic human prostate imaging. *Sci. Transl. Med.* **11**, eaav2169 (2019).
13. Park, B. et al. 3D wide-field multispectral photoacoustic imaging of human melanomas *in vivo*: a pilot study. *J. Eur. Acad. Dermatol. Venereol.* **35**, 669–676 (2021).
14. Yao, J. & Wang L. V. Photoacoustic microscopy. *Laser Photon Rev.* **7**, <https://doi.org/10.1002/lpor.201200060> (2013).
15. Maslov, K. et al. Optical-resolution photoacoustic microscopy for *in vivo* imaging of single capillaries. *Opt. Lett.* **33**, 929–931 (2008).
16. Zhang, H. F. et al. Functional photoacoustic microscopy for high-resolution and noninvasive *in vivo* imaging. *Nat. Biotechnol.* **24**, 848–851 (2006).
17. Hu, S., Maslov, K. & Wang, L. V. Second-generation optical-resolution photoacoustic microscopy with improved sensitivity and speed. *Opt. Lett.* **36**, 1134–1136 (2011).
18. Rao, B. et al. Hybrid-scanning optical-resolution photoacoustic microscopy for *in vivo* vasculature imaging. *Opt. Lett.* **35**, 1521–1523 (2010).
19. Wang, L. et al. Fast voice-coil scanning optical-resolution photoacoustic microscopy. *Opt. Lett.* **36**, 139–141 (2011).
20. Zhu, X. et al. Ultrasonic detection based on polarization-dependent optical reflection. *Opt. Lett.* **42**, 439–441 (2017).
21. Zhu, X. et al. Resolution-matched reflection mode photoacoustic microscopy and optical coherence tomography dual modality system. *Photoacoustics* **19**, 100188 (2020).
22. Wang, T. et al. Multiparametric photoacoustic microscopy of the mouse brain with 300-kHz A-line rate. *Neurophotonics* **3**, 045006–045006 (2016).
23. Kim, J. Y. et al. High-speed and high-SNR photoacoustic microscopy based on a galvanometer mirror in non-conducting liquid. *Sci. Rep.* **6**, 34803 (2016).
24. Kim, J. et al. Super-resolution localization photoacoustic microscopy using intrinsic red blood cells as contrast absorbers. *Light Sci. Appl.* **8**, 103 (2019).
25. Lee, J. et al. Fully waterproof two-axis galvanometer scanner for enhanced wide-field optical-resolution photoacoustic microscopy. *Opt. Lett.* **45**, 865–868 (2020).
26. Yao, J. et al. Wide-field fast-scanning photoacoustic microscopy based on a water-immersible MEMS scanning mirror. *J. Biomed. Opt.* **17**, 080505–080505 (2012).
27. Kim, J. Y. et al. Fast optical-resolution photoacoustic microscopy using a 2-axis water-proofing MEMS scanner. *Sci. Rep.* **5**, 7932 (2015).
28. Park, K. et al. Handheld photoacoustic microscopy probe. *Sci. Rep.* **7**, 13359 (2017).
29. Chen, Q. et al. Ultracompact high-resolution photoacoustic microscopy. *Opt. Lett.* **43**, 1615–1618 (2018).
30. Lan, B. et al. High-speed widefield photoacoustic microscopy of small-animal hemodynamics. *Biomed. Opt. Express* **9**, 4689–4701 (2018).
31. Yao, J. et al. High-speed label-free functional photoacoustic microscopy of mouse brain *in action*. *Nat. methods* **12**, 407–410 (2015).
32. Zhu, X. et al. Longitudinal intravital imaging of mouse placenta. *Sci. Adv.* **10**, eadk1278 (2024).
33. Ren, D. et al. A review of transparent sensors for photoacoustic imaging applications. *Photonics* **8**, 324 (2021).
34. Park, S. & Chang, J. H. Optically transparent ultrasound transducers for combined ultrasound and photoacoustic imaging: a review. *J. Acoust. Soc. Korea* **42**, 441–451 (2023).
35. Peng, H. et al. Photoacoustic microscopy based on transparent piezoelectric ultrasound transducers. *J. Innov. Opt. Health Sci.* **16**, 2330001 (2023).
36. Cho, S. et al. An ultrasensitive and broadband transparent ultrasound transducer for ultrasound and photoacoustic imaging *in vivo*. *Nat. Commun.* **15**, 1444 (2024).
37. Chen, R. et al. Transparent high-frequency ultrasonic transducer for photoacoustic microscopy application. *IEEE Trans. Ultrason Ferroelectr. Freq. Control* **67**, 1848–1853 (2020).
38. Chen, M. et al. High-speed wide-field photoacoustic microscopy using a cylindrically focused transparent high-frequency ultrasound transducer. *Photoacoustics* **28**, 100417 (2022).
39. Chen, H. et al. Optical-resolution photoacoustic microscopy using transparent ultrasound transducer. *Sensors* **19**, 5470 (2019).

40. Zhang, J. et al. Broadband transparent ultrasound transducer with polymethyl methacrylate as matching layer for in vivo photoacoustic microscopy. *Photoacoustics* **33**, 100548 (2023).

41. Park, B. et al. A photoacoustic fider fully integrated with a solid-state dye laser and transparent ultrasound transducer. *Photoacoustics* **23**, 100290 (2021).

42. Qiu, C. et al. Transparent ferroelectric crystals with ultrahigh piezoelectricity. *Nature* **577**, 350–354 (2020).

43. Chen, H. et al. A high sensitivity transparent ultrasound transducer based on PMN-PT for ultrasound and photoacoustic imaging. *IEEE Sens. Lett.* **5**, 1–4 (2021).

44. Fang, C., Hu, H. & Zou, J. A focused optically transparent PVDF transducer for photoacoustic microscopy. *IEEE Sens. J.* **20**, 2313–2319 (2020).

45. Kim, D. et al. An ultraviolet-transparent ultrasound transducer enables high-resolution label-free photoacoustic histopathology. *Laser Photonics Rev.* **18** (2023).

46. Liang, Y. et al. Fast-scanning photoacoustic microscopy with a side-looking fiber optic ultrasound sensor. *Biomed. Opt. Express* **9**, 5809–5816 (2018).

47. Allen, T. J. et al. Ultrafast laser-scanning optical resolution photoacoustic microscopy at up to 2 million A-lines per second. *J. Biomed. Opt.* **23**, 126502–126502 (2018).

48. Yang, J. et al. Motionless volumetric photoacoustic microscopy with spatially invariant resolution. *Nat. Commun.* **8**, 780 (2017).

49. Edward, Z. Z. & Paul, C. B. Characteristics of optimized fibre-optic ultrasound receivers for minimally invasive photoacoustic detection. *Proc. SPIE* **9323**, 932311 (2015).

50. Guggenheim, J. A. et al. Ultrasensitive plano-concave optical microresonators for ultrasound sensing. *Nat. Photonics* **11**, 714–719 (2017).

51. Hajireza, P. et al. Non-interferometric photoacoustic remote sensing microscopy. *Light Sci. Appl.* **6**, e16278 (2017).

52. Lee, C. et al. In vitro photoacoustic measurement of hemoglobin oxygen saturation using a single pulsed broadband supercontinuum laser source. *Appl. Opt.* **53**, 3884–3889 (2014).

53. Billeh, Y. N., Liu, M. & Buma, T. Spectroscopic photoacoustic microscopy using a photonic crystal fiber supercontinuum source. *Opt. express* **18**, 18519–18524 (2010).

54. Lee, C. et al. Combined photoacoustic and optical coherence tomography using a single near-infrared supercontinuum laser source. *Appl. Opt.* **52**, 1824–1828 (2013).

55. Shu, X. et al. Single all-fiber-based nanosecond-pulsed supercontinuum source for multispectral photoacoustic microscopy and optical coherence tomography. *Opt. Lett.* **41**, 2743–2746 (2016).

56. Chang, Y. et al. Co-impulse multispectral photoacoustic microscopy and optical coherence tomography system using a single supercontinuum laser. *Opt. Lett.* **44**, 4459–4462 (2019).

57. Dasa, M. K. et al. All-fibre supercontinuum laser for in vivo multispectral photoacoustic microscopy of lipids in the extended near-infrared region. *Photoacoustics* **18**, 100163 (2020).

58. Koeplinger, D., Liu M. & Buma, T. Photoacoustic microscopy with a pulsed multi-color source based on stimulated Raman scattering. in *2011 IEEE International Ultrasonics Symposium*. (IEEE, 2011)

59. Hajireza, P., Forbrich, A. & Zemp, R. In-vivo functional optical-resolution photoacoustic microscopy with stimulated Raman scattering fiber-laser source. *Biomed. Opt. express* **5**, 539–546 (2014).

60. Liang, Y. et al. 2 MHz multi-wavelength pulsed laser for functional photoacoustic microscopy. *Opt. Lett.* **42**, 1452–1455 (2017).

61. Chen, J. et al. Wide-field polygon-scanning photoacoustic microscopy of oxygen saturation at 1-MHz A-line rate. *Photoacoustics* **20**, 100195 (2020).

62. Liu, C. et al. Five-wavelength optical-resolution photoacoustic microscopy of blood and lymphatic vessels. *Adv. Photonics* **3**, 016002 (2021).

63. Zhu, X. et al. Real-time whole-brain imaging of hemodynamics and oxygenation at micro-vessel resolution with ultrafast wide-field photoacoustic microscopy. *Light Sci. Appl.* **11**, 138 (2022).

64. Song, L., Maslov, K. & Wang, L. V. Multifocal optical-resolution photoacoustic microscopy in vivo. *Opt. Lett.* **36**, 1236–1238 (2011).

65. Li, G., Maslov, K. I. & Wang, L. V. Reflection-mode multifocal optical-resolution photoacoustic microscopy. *J. Biomed. Opt.* **18**, 030501–030501 (2013).

66. Xia, J. et al. Wide-field two-dimensional multifocal optical-resolution photoacoustic-computed microscopy. *Opt. Lett.* **38**, 5236–5239 (2013).

67. Imai, T. et al. High-throughput ultraviolet photoacoustic microscopy with multifocal excitation. *J. Biomed. Opt.* **23**, 036007–036007 (2018).

68. Chen, Z. et al. Multifocal structured illumination optoacoustic microscopy. *Light. Sci. Appl.* **9**, 152 (2020).

69. Li, Y. et al. Snapshot photoacoustic topography through an ergodic relay for high-throughput imaging of optical absorption. *Nat. Photonics* **14**, 164–170 (2020).

70. Li, Y. et al. Multifocal photoacoustic microscopy using a single-element ultrasonic transducer through an ergodic relay. *Light Sci. Appl.* **9**, 135 (2020).

71. Rajanna, A. R. et al. Prostate cancer detection using photoacoustic imaging and deep learning. *Electron. Imaging* **28**, 1–6 (2016).

72. Davoudi, N., Deán-Ben, X. L. & Razansky, D. Deep learning optoacoustic tomography with sparse data. *Nat. Mach. Intell.* **1**, 453–460 (2019).

73. Hauptmann, A. et al. Model-based learning for accelerated, limited-view 3-D photoacoustic tomography. *IEEE Trans. Med. Imaging* **37**, 1382–1393 (2018).

74. Vu, T. et al. A generative adversarial network for artifact removal in photoacoustic computed tomography with a linear-array transducer. *Exp. Biol. Med.* **245**, 597–605 (2020).

75. Vu, T. et al. Deep image prior for undersampling high-speed photoacoustic microscopy. *Photoacoustics* **22**, 100266 (2021).

76. Zhou, J. et al. Photoacoustic microscopy with sparse data by convolutional neural networks. *Photoacoustics* **22**, 100242 (2021).

77. DiSpirito, A. et al. Reconstructing undersampled photoacoustic microscopy images using deep learning. *IEEE Trans. Med. Imaging* **40**, 562–570 (2020).

78. Seong, D. et al. Three-dimensional reconstructing undersampled photoacoustic microscopy images using deep learning. *Photoacoustics* **29**, 100429 (2023).

79. Hu, S. & Wang, L. V. Photoacoustic imaging and characterization of the microvasculature. *J. Biomed. Opt.* **15**, 011101 (2010).

80. Attia, A. B. E. et al. A review of clinical photoacoustic imaging: current and future trends. *Photoacoustics* **16**, 100144 (2019).

81. Cho, S. W. et al. Sounding out the dynamics: a concise review of high-speed photoacoustic microscopy. *J. Biomed. Opt.* **29**, S11521 (2024).

82. Das, D. et al. Another decade of photoacoustic imaging. *Phys. Med. Biol.* **66**, 05TR01 (2021).

83. Steinberg, I. et al. Photoacoustic clinical imaging. *Photoacoustics* **14**, 77–98 (2019).

84. Zhu, X. Chen M., & Yao J. Photoacoustic Microscopy, in *Biomedical Optical Imaging: From Nanoscopy to Tomography*, (eds Xia, J. and Choe, R.) (AIP Publishing LLC, 0, 2014).

85. Malonek, D. & Grinvald, A. Interactions between electrical activity and cortical microcirculation revealed by imaging spectroscopy: implications for functional brain mapping. *Science* **272**, 551–554 (1996).

86. Logothetis, N. K. What we can do and what we cannot do with fMRI. *Nature* **453**, 869–878 (2008).

87. Hu, S. & Wang, L. V. Neurovascular photoacoustic tomography. *Front. Neuroenergetics* **2**, 10 (2010).

88. Zafar, M. et al. Spiral laser scanning photoacoustic microscopy for functional brain imaging in rats. *Neurophotonics* **11**, 015007 (2024).

89. Lin, L. et al. High-speed photoacoustic microscopy of mouse cortical microhemodynamics. *J. Biophotonics* **10**, 792–798 (2017).

90. He, Y. et al. Wave of single-impulse-stimulated fast initial dip in single vessels of mouse brains imaged by high-speed functional photoacoustic microscopy. *J. Biomed. Opt.* **25**, 1–11 (2020).

91. Zhang, D. et al. Epinephrine-induced effects on cerebral microcirculation and oxygenation dynamics using multimodal monitoring and functional photoacoustic microscopy. *Anesthesiology* **139**, 173–185 (2023).

92. Huang, D. et al. Three-dimensional label-free imaging of mammalian yolk sac vascular remodeling with optical resolution photoacoustic microscopy. *Photoacoustics* **17**, 100152 (2020).

93. Qu, Y. et al. Transvaginal fast-scanning optical-resolution photoacoustic endoscopy. *J. Biomed. Opt.* **23**, 1–4 (2018).

94. Rao, B. et al. Optical resolution photoacoustic microscopy of ovary and fallopian tube. *Sci. Rep.* **9**, 14306 (2019).

95. Kittler, H. et al. Diagnostic accuracy of dermoscopy. *Lancet Oncol.* **3**, 159–165 (2002).

96. Aguirre, J. et al. Precision assessment of label-free psoriasis biomarkers with ultra-broadband optoacoustic mesoscopy. *Nat. Biomed. Eng.* **1**, 0068 (2017).

97. Aguirre, J. et al. Motion quantification and automated correction in clinical RSOM. *IEEE Trans. Med. Imaging* **38**, 1340–1346 (2019).

98. Aguirre, J. et al. Broadband mesoscopic optoacoustic tomography reveals skin layers. *Opt. Lett.* **39**, 6297–6300 (2014).

99. Zabihian, B. et al. In vivo dual-modality photoacoustic and optical coherence tomography imaging of human dermatological pathologies. *Biomed. Opt. Express* **6**, 3163–3178 (2015).

100. Xu, Z. et al. Visualizing tumor angiogenesis and boundary with polygon-scanning multiscale photoacoustic microscopy. *Photoacoustics* **26**, 100342 (2022).

101. Ahn, J. et al. Fully integrated photoacoustic microscopy and photoplethysmography of human *in vivo*. *Photoacoustics* **27**, 100374 (2022).

102. Ahn, J. et al. High-resolution functional photoacoustic monitoring of vascular dynamics in human fingers. *Photoacoustics* **23**, 100282 (2021).

103. Cao, R. et al. Label-free intraoperative histology of bone tissue via deep-learning-assisted ultraviolet photoacoustic microscopy. *Nat. Biomed. Eng.* **7**, 124–134 (2023).

104. Shi, J. et al. High-resolution, high-contrast mid-infrared imaging of fresh biological samples with ultraviolet-localized photoacoustic microscopy. *Nat. Photonics* **13**, 609–615 (2019).

105. Wong, T. T. W. et al. Fast label-free multilayered histology-like imaging of human breast cancer by photoacoustic microscopy. *Sci. Adv.* **3**, e1602168 (2017).

106. Kim, H. & Chang, J. H. Multimodal photoacoustic imaging as a tool for sentinel lymph node identification and biopsy guidance. *Biomed. Eng. Lett.* **8**, 183–191 (2018).

107. Brendon, S. R. et al. Prostate needle biopsy metabolic analysis and virtual H&E microscopy using photoacoustic remote sensing and autofluorescence microscopy (Conference Presentation). in *Proc. SPIE*. 2023.

108. Ma, H. et al. Switchable optical and acoustic resolution photoacoustic dermoscope dedicated into *in vivo* biopsy-like of human skin. *Appl. Phys. Lett.* **116**, 073703 (2020).

109. Li, X. et al. High-speed label-free ultraviolet photoacoustic microscopy for histology-like imaging of unprocessed biological tissues. *Opt. Lett.* **45**, 5401–5404 (2020).

110. Wong, T. T. W. et al. Label-free automated three-dimensional imaging of whole organs by microtomy-assisted photoacoustic microscopy. *Nat. Commun.* **8**, 1386 (2017).

111. Galanzha, E. I. & Zharov, V. P. Photoacoustic flow cytometry. *Methods* **57**, 280–296 (2012).

112. Galanzha, E. I. et al. In vivo liquid biopsy using cytophone platform for photoacoustic detection of circulating tumor cells in patients with melanoma. *Sci. Transl. Med.* **11**, eaat5857 (2019).

113. Galanzha, E. I. et al. In vivo magnetic enrichment and multiplex photoacoustic detection of circulating tumour cells. *Nat. Nanotechnol.* **4**, 855–860 (2009).

114. He, Y. et al. In vivo label-free photoacoustic flow cytography and on-the-spot laser killing of single circulating melanoma cells. *Sci. Rep.* **6**, 39616 (2016).

115. Galanzha, E. I. et al. In vivo acoustic and photoacoustic focusing of circulating cells. *Sci. Rep.* **6**, 21531 (2016).

116. Nedosekin, D. A. et al. Photoacoustic and photothermal detection of circulating tumor cells, bacteria and nanoparticles in cerebrospinal fluid *in vivo* and *ex vivo*. 523–533 (Wiley Online Library, 2013).

117. Taboada, C. et al. Glassfrogs conceal blood in their liver to maintain transparency. *Science* **378**, 1315–1320 (2022).

118. Chen, S. L., Guo, L. J. & Wang, X. All-optical photoacoustic microscopy. *Photoacoustics* **3**, 143–150 (2015).

119. Dong, B., Sun, C. & Zhang, H. F. Optical detection of ultrasound in photoacoustic imaging. *IEEE Trans. Biomed. Eng.* **64**, 4–15 (2017).

120. Li, Z. et al. Broadband and ultrasensitive graphene-based mechanical wave detector with nanosecond response used for biological photoacoustic imaging. *ACS Appl. Mater. Interfaces* **12**, 17268–17275 (2020).

121. Zhu, X. et al. Polarization-dependent optical reflection ultrasonic detection. *Proc. SPIE* **10064**, 100641X (2017).

122. Zhu, X. et al. High-speed wide-field functional photoacoustic microscopy of mouse brain actions. *Proc. SPIE* **PC11960**, PC119600Z (2022).

123. Chen, Q. et al. Progress of clinical translation of handheld and semi-handheld photoacoustic imaging. *Photoacoustics* **22**, 100264 (2021).

124. Chen, J. et al. Freehand scanning photoacoustic microscopy with simultaneous localization and mapping. *Photoacoustics* **28**, 100411 (2022).

125. Chen, Z. et al. Multimodal optoacoustic imaging: methods and contrast materials. *Chem. Soc. Rev.* **53**, 6068–6099 (2024).

126. Martell, M. T., Haven, N. J. M. & Zemp, R. J. Multimodal imaging with spectral-domain optical coherence tomography and photoacoustic remote sensing microscopy. *Opt. Lett.* **45**, 4859–4862 (2020).

127. Nguyen, V. P. et al. Chain-like gold nanoparticle clusters for multimodal photoacoustic microscopy and optical coherence tomography enhanced molecular imaging. *Nat. Commun.* **12**, 34 (2021).

128. Zafar, M. et al. Skin imaging using optical coherence tomography and photoacoustic imaging: a mini-review. *Optics* **5**, 248–266 (2024).

129. Zhang, W. et al. Simultaneous photoacoustic microscopy, spectral-domain optical coherence tomography, and fluorescein microscopy multi-modality retinal imaging. *Photoacoustics* **20**, 100194 (2020).

130. Hai, P. et al. Near-infrared optical-resolution photoacoustic microscopy. *Opt. Lett.* **39**, 5192–5195 (2014).

131. Horstmeyer, R., Ruan, H. & Yang, C. Guidestar-assisted waveform-shaping methods for focusing light into biological tissue. *Nat. photonics* **9**, 563–571 (2015).

132. Lin, Q. et al. Acoustic hologram-induced virtual *in vivo* enhanced waveguide (AH-VIEW). *Sci. Adv.* **10**, eadl2232 (2024).

Acknowledgements

This work was partially sponsored by the United States National Institutes of Health (NIH) grants R21EB027981, R21 EB027304, RF1 NS115581, R01 NS111039, R01 EB028143, R01 DK139109; The United States National Science Foundation (NSF) CAREER award 2144788; Duke University Pratt

Beyond the Horizon Grant; Eli Lilly Research Award Program; and Chan Zuckerberg Initiative Grant (2020-226178).

Author contributions

J.Y. conceived and directed the project. X.Z. drafted the manuscript. J.Y., L.M., S.W.C, and X.Z. revised the manuscript.

Competing interests

The authors declare no competing interests.

Additional information

Correspondence and requests for materials should be addressed to Junjie Yao.

Reprints and permissions information is available at

<http://www.nature.com/reprints>

Publisher's note Springer Nature remains neutral with regard to jurisdictional claims in published maps and institutional affiliations.

Open Access This article is licensed under a Creative Commons Attribution-NonCommercial-NoDerivatives 4.0 International License, which permits any non-commercial use, sharing, distribution and reproduction in any medium or format, as long as you give appropriate credit to the original author(s) and the source, provide a link to the Creative Commons licence, and indicate if you modified the licensed material. You do not have permission under this licence to share adapted material derived from this article or parts of it. The images or other third party material in this article are included in the article's Creative Commons licence, unless indicated otherwise in a credit line to the material. If material is not included in the article's Creative Commons licence and your intended use is not permitted by statutory regulation or exceeds the permitted use, you will need to obtain permission directly from the copyright holder. To view a copy of this licence, visit <http://creativecommons.org/licenses/by-nc-nd/4.0/>.

© The Author(s) 2024